Cell Biomaterials

Article

# Adipose-mimetic granular hydrogels uncover biophysical cues driving breast cancer invasion

## Graphical abstract

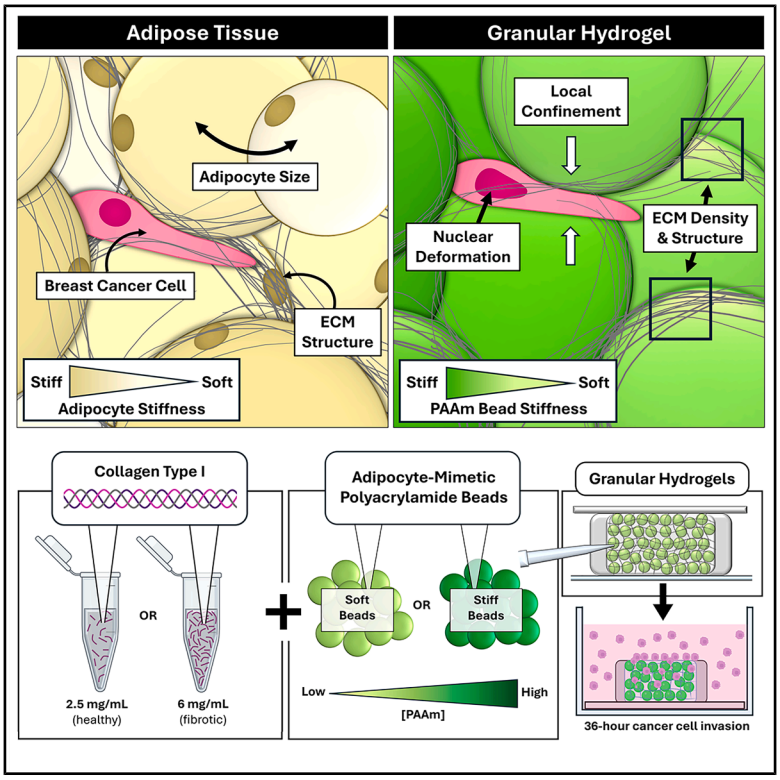


## Highlights

- Elastically tunable polyacrylamide beads recapitulate primary adipocyte mechanics
- Adipocyte-like structures coordinate extracellular matrix organization in adipose tissue
- Adipocyte mechanics regulate cancer cell invasion in a stiffness-dependent manner

## Authors

Brianna K. Knode, Garrett F. Beeghly, Brittany E. Schutrum, ..., Salvatore Girardo, Corey S. O'Hern, Claudia Fischbach

## Correspondence

cf99@cornell.edu

## In brief

In the initial stages of metastatic breast cancer, tumor cells invade through fatty breast tissue; however, it is unclear how the structure of this tissue regulates cancer progression. Here, we fabricate a tunable synthetic tissue culture platform that replicates mammary adipose structure and seed these hydrogels with breast cancer cells to study the invasion process. Data collected from this platform suggest that adipocyte mechanics regulate cancer invasion in a stiffness-dependent manner by coordinating both extracellular matrix architecture and cellular confinement.

Knode et al., 2026, Cell Biomaterials 2, 100411
August 18, 2026 
https://doi.org/10.1016/j.celbio.2026.100411

CellPress

Please cite this article in press as: Knode et al., Adipose-mimetic granular hydrogels uncover biophysical cues driving breast cancer invasion, Cell Biomaterials (2026), https://doi.org/10.1016/j.celbio.2026.100411

Cell Biomaterials

CellPress

Article

# Adipose-mimetic granular hydrogels uncover biophysical cues driving breast cancer invasion

Brianna K. Knode,[1,2] Garrett F. Beeghly,[1] Brittany E. Schutrum,[1] Dong Wang,[3] Yitong Zheng,[3,4] Alice Battistella,[5] Ruchi Goswami,[5] Chi-Yong Eom,[1] Irina Kopyeva,[1] Aline Bozec,[6,7] Jochen Guck,[5] Nozomi Nishimura,[1] Salvatore Girardo,[5] Corey S. O'Hern,[3,4,8] and Claudia Fischbach[1,9,*]

[1]Nancy E. and Peter C. Meinig School of Biomedical Engineering, Cornell University, Ithaca, NY, USA
[2]Graduate Program in Biomedical and Biological Sciences, Cornell University, Ithaca, NY, USA
[3]Department of Mechanical Engineering, Yale University, New Haven, CT, USA
[4]Integrated Graduate Program in Physical and Engineering Biology, Yale University, New Haven, CT, USA
[5]Max Planck Institute for the Science of Light & Max-Planck-Zentrum für Physik und Medizin, Erlangen, Germany
[6]Department of Internal Medicine 3 – Rheumatology and Immunology, Friedrich-Alexander University Erlangen-Nürnberg and Universitätsklinikum Erlangen, 91054 Erlangen, Germany
[7]Deutsches Zentrum für Immuntherapie, Friedrich-Alexander University Erlangen-Nürnberg and Universitätsklinikum Erlangen, 91054 Erlangen, Germany
[8]Department of Physics, Yale University, New Haven, CT, USA
[9]Lead contact
*Correspondence: cf99@cornell.edu
https://doi.org/10.1016/j.celbio.2026.100411

**THE BIGGER PICTURE** Approximately one in eight women will develop breast cancer in their lifetime, and metastatic breast cancer is the leading cause of cancer-related death in women worldwide. In the first steps of metastasis, cancer cells invade out of the glandular structures of breast tissue and into the surrounding adipose tissue-rich mammary stroma. While mechanical properties of the tumor microenvironment are known to regulate invasion, the role of adipose tissue mechanics, which are shaped largely by adipocytes and their surrounding extracellular matrix (ECM), remains poorly understood. This knowledge gap arises, in part, from a lack of appropriate model systems that replicate the mechanical properties of primary adipocytes. Moreover, no methods currently exist to decouple the effects of adipocyte physical and biochemical properties for investigation. To address these shortcomings, we developed an *in vitro* model system to identify how adipocyte size and stiffness affect ECM microarchitecture and leveraged this system to evaluate breast cancer cell migration through structurally heterogeneous engineered tissue conditions. First, we quantified the heterogeneous size and stiffness of primary adipocytes and replicated these properties by fabricating adipocyte-sized polyacrylamide (PAAm) beads with tunable elasticity. Subsequently, we embedded these beads into type I collagen, the primary fibrillar ECM component of breast adipose tissue, to form 3D granular hydrogels mimicking aspects of native adipose tissue architecture. When seeded with breast cancer cells, invasion was more pronounced in soft bead hydrogels, whereas stiffer beads physically restricted tumor cell migration, an effect that also correlated with increased ECM fiber alignment. Taken together, these findings suggest that adipocyte physical properties regulate tumor invasion by coordinating ECM architecture and cellular confinement. Ultimately, this work highlights the utility of tunable PAAm bead-collagen composites as micromechanical models to study the effect of adipose tissue structure on cancer cell invasion.

## SUMMARY

Breast cancer cells invade collagen type I-rich mammary adipose tissue during the initial stages of metastasis, but how adipocyte mechanics regulate this process remains unclear. To elucidate these connections, we quantified the size and stiffness of primary adipocytes and replicated these properties using tunable polyacrylamide (PAAm) beads. Subsequently, we embedded these beads into type I collagen to form 3D granular hydrogels mimicking native adipose tissue architecture. Bead-embedded hydrogels demonstrated increased breast cancer cell invasion and collagen fiber organization relative to beadless controls, and cells

Please cite this article in press as: Knode et al., Adipose-mimetic granular hydrogels uncover biophysical cues driving breast cancer invasion, Cell Biomaterials (2026), https://doi.org/10.1016/j.celbio.2026.100411



invaded more readily in systems with decreased bead stiffness. Similarly, discrete element method simulations revealed that soft beads promoted invasion by deforming in response to confined cancer cell migration. These trends were validated *in vivo* via intravital imaging of murine mammary tumors. Collectively, our data suggest that adipocyte mechanics regulate breast cancer invasion by coordinating both matrix architecture and cellular confinement.

## INTRODUCTION

Metastatic breast cancer is the leading cause of cancer-related death in women worldwide.[1] Despite decades of progress, our ability to diagnose and treat metastatic breast cancer remains limited due to an incomplete understanding of how cancer cells invade. Although most breast cancers originate in the mammary ducts and lobules,[2] metastasis begins when cancer cells escape these epithelial structures and migrate into the surrounding adipose tissue-rich host microenvironment.[3,4] They do so by squeezing between stromal structures, either as single cells or collective strands,[5,6] to reach blood vessels and ultimately colonize distant organs.[7] While previous studies have investigated how adipose tissue influences tumor cell phenotype through biochemical cues,[8–10] the role of its distinctive biophysical properties, which may be equally important, remains less clear.

About 85 percent of adipose tissue by volume is comprised of adipocytes, which are structurally and functionally unique due to their large size, spherical morphology, and lack of cell motility.[11,12] To support their roles in energy storage and thermoregulation, namely facilitating dynamic lipid loss and uptake during metabolism, adipocytes also exhibit physical and mechanical heterogeneity.[13–16] Notably, in metabolically altered states such as obesity and diabetes, adipocytes can adopt abnormal mechanical phenotypes.[15,17] Adding to this physical complexity, mammary adipocytes are surrounded by a network of extracellular matrix (ECM) primarily composed of fibrillar collagen type I,[18] which cancer cells navigate during invasion. In obesity, this collagen network becomes denser and more aligned,[19,20] which has been shown to promote tumor cell invasion in other contexts by influencing cell adhesion and physical confinement.[20–23] However, the relationship between adipocyte mechanics, ECM architecture, and breast cancer invasion remains poorly understood due, in part, to a lack of model systems capable of capturing the interplay between these different parameters in a tractable manner.

Most *in vitro* studies of adipose tissue employ one of three tissue culture methods, each with intrinsic limitations.[24] Most commonly, adipocytes are pre-differentiated from progenitor cells, but these cells do not develop the large and unilocular phenotypes characteristic of mature adipocytes and fail to recapitulate the mechanics of primary tissues.[15] By contrast, primary adipocytes exhibit the native structure and properties of the tissue from which they are resected but are notoriously difficult to culture due to their buoyancy and fragility.[25] Moreover, isolated primary adipocytes[26,27] and whole adipose tissue explants[28] experience rapid phenotype loss, limiting their suitability for extended *in vitro* studies and manipulation of mechanical properties. Hence, no suitable methods currently exist to recapitulate the key mechanical and structural properties of native adipose tissue, motivating the need for innovative model systems to examine their effects on cancer cell invasion independently of biochemical signals.

While the physical characteristics of complex tissues are often modeled using homogeneous bulk hydrogels,[29] granular hydrogels consisting of tunable microgel particles offer functional advantages.[30–39] For example, granular hydrogels demonstrate inherent porosity, control over hydrogel structure by adjusting particle packing density, and the ability to curate functionally diverse synthetic tissues via selective particle functionalization and interparticle crosslinking.[30,31,37–40] Artificially crosslinked packings of hydrogel particles are most commonly used to engineer tissues for regenerative approaches and study constituent cell dynamics.[32–35,40] In addition, some systems have combined hydrogel particles with ECM components[36,39] or have tested the effect of cell packing or particle size on cancer growth.[38,39] However, how collagen network microarchitecture is controlled in such granular systems and the effects these changes have on invasion at varied bead stiffnesses have yet to be investigated. Consequentially, the fundamental relationships between adipocyte mechanics, fibrillar matrix architecture, and mammary cancer invasion remain unclear.

To model the discrete and continuous physical characteristics of adipose tissue, we designed adipocyte-sized hydrogel granules and embedded them into collagen type I at a physiologically relevant volume ratio. We first measured the effective diameter and stiffness of primary adipocytes and then recapitulated these parameters with adipocyte-mimetic polyacrylamide (PAAm) beads, yielding biocompatible, cell-scale mechanical models with spherical morphology and mechanical tunability.[41,42] Moreover, incorporation of the beads into collagen I allowed us to replicate bulk adipose tissue organization and identify how adipocyte packing impacts collagen. Finally, we applied this biphasic model to experimentally and computationally investigate the role of both adipocyte and ECM mechanics on tumor cell migration, and validated our findings by investigating mammary tumor invasion in a syngeneic mouse model using intravital imaging. By mimicking adipose tissue's biophysical traits, granular collagen hydrogels offer insights into how local stiffness and structure regulate cancer cell invasion. As adipose infiltration can influence cell function in various other contexts, including metabolic diseases, our model provides a broadly applicable platform to study these connections.

## RESULTS

### Tunable PAAm beads recapitulate primary adipocyte size and stiffness

Primary adipocytes and a collagen-rich ECM constitute the primary structural components of adipose tissue in the breast[11,12]

Please cite this article in press as: Knode et al., Adipose-mimetic granular hydrogels uncover biophysical cues driving breast cancer invasion, Cell Biomaterials (2026), https://doi.org/10.1016/j.celbio.2026.100411



CellPress

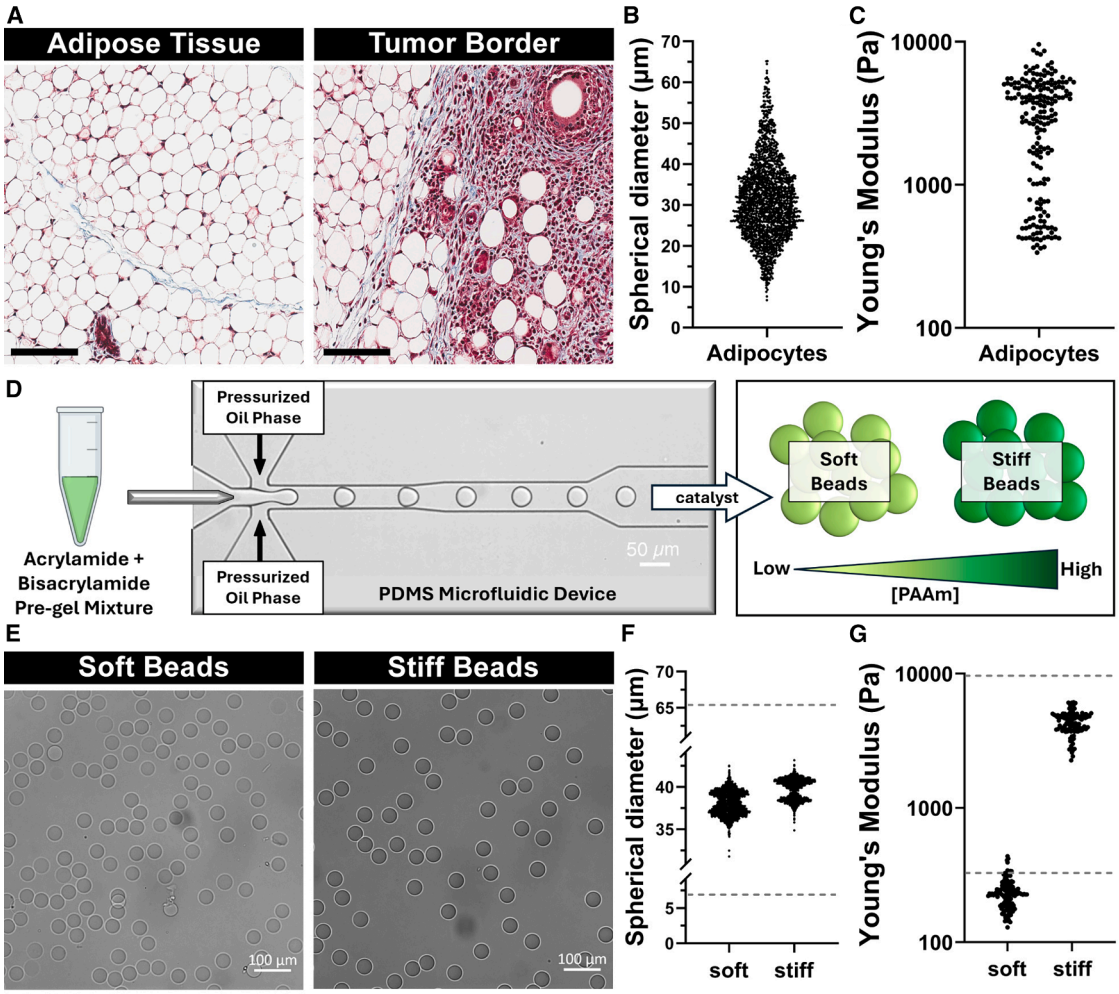


**Figure 1. Tunable PAAm beads recapitulate primary adipocyte size and stiffness**

(A) Masson's trichrome staining of murine adipose tissue; scale bar, 100 μm.

(B) Murine adipocyte diameter distribution.

(C) AFM analysis of murine adipocyte stiffness distribution.

(D) Schematic of tunable PAAm bead fabrication via custom droplet microfluidics.

(E) Bright-field images of soft and stiff PAAm bead batches; scale bar, 100 μm.

(F) PAAm bead diameter distributions, dashed lines represent adipocyte range.

(G) AFM analysis of PAAm bead stiffnesses, and dashed lines represent the adipocyte range. Intensity and contrast of figure micrographs have been altered for visualization purposes.

(Figure 1A, left). During tumor invasion, breast cancer cells at the invasion front must physically navigate this environment, migrating through the interstitial spaces between individual adipocytes as single cells or in small clusters[5] (Figure 1A, right). To better understand adipocyte size and deformability as two biophysical features that influence tumor cell migration, we first analyzed histological sections of mammary fat pads collected from female C57BL/6 mice (Figure 1A, left). We observed substantial heterogeneity in the relative size and deformation of densely packed adipocytes and characterized the cross-sectional areas $A$ of individual adipocytes to estimate cell diameters ($A = \pi\left(\frac{d}{2}\right)^2$). Effective diameters ranged from d = 6.70 μm to 65.2 μm, with a mean $\langle d \rangle = 31.2$ μm and standard deviation (SD) $\Delta d = 9.78$ μm (Figure 1B). To confirm that these two-dimensional (2D) size measurements could be used to approximate three-dimensional (3D) trends, we show that $\langle d \rangle$ is monotonically related to the true average diameter of the adipocytes, $\langle D \rangle$, and the SD $\sigma_d$ of d is proportional to the SD $\sigma_D$ of true diameter $D$ (Figure S1A). In addition, we isolated primary adipocytes from a subset of resected murine tissue[43] for mechanical characterization via atomic force microscopy (AFM), immobilizing the cells on the imaging substrate during data acquisition (setup shown in Figure S1B). Mirroring the qualitative observation of variable adipocyte deformation in tissue sections, we found primary adipocyte stiffness to be considerably heterogeneous, with the

elastic moduli of cells ranging from a few hundred to several thousand pascals (Figures 1C and S1C). This broad range of values additionally aligns with the mechanical variability previously observed with other adipose model systems, though our measurements ranged from similar (100–1,000 Pa) to an order of magnitude greater than (~10,000 Pa) previous reports, which used differentiated preadipocyte cell lines[14,15,44] or long-term explanted adipocyte cultures.[45] These include a study that used the specific AFM protocol and parameters employed in this report,[15] suggesting that our findings are not an artifact of the method but a true feature of the tissue. Collectively, our results reflect an inherent variability of adipocyte stiffness, warranting further investigation into how this heterogeneity influences breast cancer invasion.

To develop a micromechanical, adipose tissue-mimetic model informed by our analysis of adipocyte size and stiffness, we next replicated the physical properties of adipocytes with biochemically inert PAAm beads. While other granular hydrogel systems employ materials such as bovine serum albumin (BSA)-stabilized oil microdroplets[39] or gelatin methacryloyl (GelMA),[38] we opted to fabricate our beads using PAAm for several reasons: it lacks bioactive cues that may independently influence cell behavior, its mechanical properties are selectively tunable, and it is comparatively more resistant to degradation over time.[46,47] We generated these beads using a customizable flow-focusing droplet microfluidic device and restricted the resulting microgel size to ~35 μm in diameter, mimicking primary adipocytes, via selective control of the oil phase flow rate. Moreover, bead stiffnesses of about 200 Pa (soft adipocytes) and 4,000 Pa (stiff adipocytes), hereinafter referred to as soft and stiff beads, respectively, were achieved by altering the concentration of fixed-ratio acrylamide monomers prior to polymerization within a catalyst-containing oil phase[41,42] (Figure 1D). Using this platform, we were able to generate bead populations of variable stiffness while maintaining nearly monodisperse size distribution (Figure 1E), achieving average diameters comparable to primary adipocytes (Figure 1F). Moreover, AFM characterization of the two bead populations confirmed that their elastic moduli were reflective of the lower (soft beads, $\langle Y \rangle$ = 230 Pa ± 60 Pa) and upper (stiff beads, $\langle Y \rangle$ = 4,339 Pa ± 845 Pa) ends of the stiffness values measured for primary adipocytes (Figure 1G). Collectively, these results demonstrate our ability to generate distinct adipocyte-sized populations of PAAm beads with elastic moduli spanning the stiffness heterogeneity of primary adipocytes.

## PAAm bead granular hydrogels model the structural organization of adipose tissue

After validating that PAAm microgels can mimic the physical properties of primary murine adipocytes, we next characterized the ECM structure of native adipose tissue. Second harmonic generation (SHG) microscopy of both human and murine adipose tissue showed organized collagen fibers occupying the interstitial spaces between individual adipocytes (Figure 2A), an arrangement necessary for tumor cell invasion.[21,48] These fibers are primarily comprised of collagen I, which accounts for about 80% of total collagen in healthy mammary tissue and is known to increase in density in cases of metastatic breast cancer.[49,50] To recreate this microarchitecture, we encapsulated soft or stiff PAAm beads in either a 2.5 or 6.0 mg/mL type I collagen hydrogel, reflective of healthy or fibrotic breast tissue phenotypes, respectively.[9,51,52] To this end, bead-laden collagen hydrogels, referred to as "granular hydrogels," were cold cast into custom polydimethylsiloxane (PDMS) microwells, as previously described,[53] to encourage collagen fibrillogenesis representative of native ECM microarchitecture (Figure 2B). To develop these granular hydrogels, we trialed collagen-to-bead volume ratios of 1:3, 1:6, and 1:9, and used a 1:6 ratio for all future experiments, as this yielded the packing fraction closest to native adipose tissue[11] while still maintaining sufficient collagen content to ensure the structural integrity of the hydrogel (Figures S2A and S2B). It is important, therefore, to note that these granular gels may not recapitulate the organization of the most tightly packed adipocytes *in vivo*, and some differences in *in vitro* cell behaviors may be attributed to this packing fraction disparity. Several studies, in fact, have demonstrated the importance of packing fraction in cell migration,[31,39,54] further motivating our use of a consistent, physiologically relevant ratio in this granular system. Confocal imaging revealed that interconnected networks of collagen fibers formed between fluorescently labeled PAAm beads, yielding architectures reminiscent of interstitial adipose ECM *in vivo* (Figure 2C). While the local bead packing fraction varied within and between individual gels, no global differences were detected across the four combinations of bead stiffness and collagen concentration tested (Figures 2D and 2E). Hence, any differences detected in subsequent experiments can be attributed to the inherent mechanical properties of the hydrogel rather than differences in porosity. We then confirmed that incorporation of PAAm beads did not impact the concentration of the interstitial collagen phase compared with respective beadless hydrogels (Figure 2F) using an adapted version of a commercially available bicinchoninic acid (BCA) assay (Figures S2C–S2E). These results ensured that any differences in data collected from the granular hydrogels are not due to variation in collagen density between conditions.

Finally, we tested the rheological properties of the granular hydrogels. As expected, 6 mg/mL collagen controls had significantly higher bulk storage moduli than 2.5 mg/mL collagen gels. Unsurprisingly, the addition of PAAm beads to either condition produced softer gels, as the fraction of collagen per volume is much lower, despite locally (in between beads) being the same (Figure S3B). The stiffness of the beads did not significantly alter the storage modulus in granular gels. Our results are in agreement with previous studies measuring adipose tissue mechanics, which found human peritoneal adipose tissue to be within 100–1,000 Pa.[39,55] Stress relaxation tests were performed at 15% strain, as this is within the range of strain generated by cells in 3D matrices.[56] Generally, granular gels were faster stress relaxing than control collagen gels, except for the 6 mg/mL collagen with stiff beads condition, which had similar stress relaxation times (~10 s) as the collagen-only controls (Figures S3C and S3D). 2.5 mg/mL gels with either type of beads exhibited the fastest stress relaxation profiles (>1 s). While these values are smaller than what has been reported for adipose tissue,[57] this can likely be explained by the lack of covalent crosslinking in our system (our system relies purely on physical crosslinking of collagen), as opposed to native tissue, which would

Please cite this article in press as: Knode et al., Adipose-mimetic granular hydrogels uncover biophysical cues driving breast cancer invasion, Cell Biomaterials (2026), https://doi.org/10.1016/j.celbio.2026.100411



CellPress

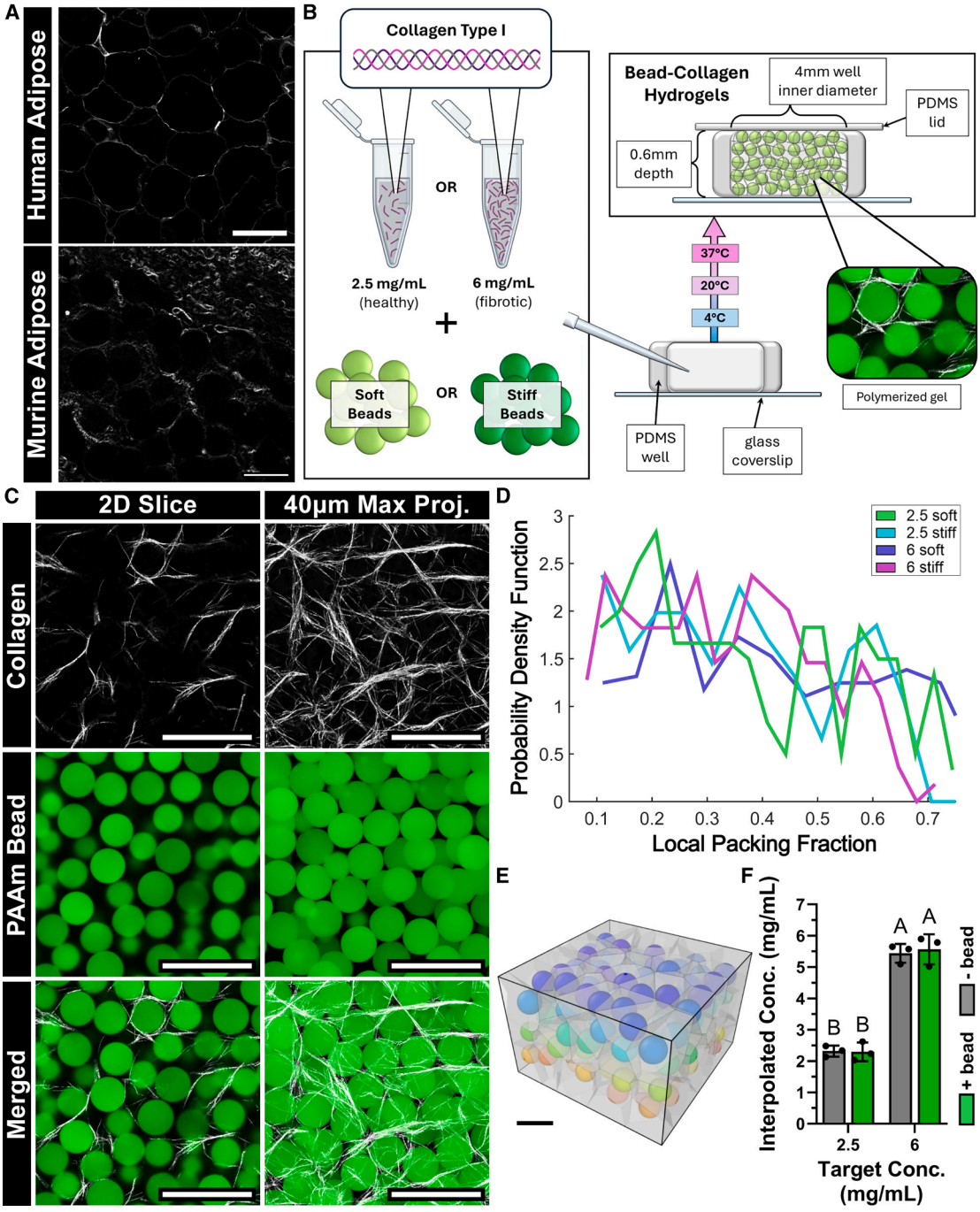


**Figure 2. PAAm bead granular hydrogels model the structural organization of adipose tissue**

(A) SHG images of interstitial ECM in whole human and murine adipose tissue; scale bar, 100 μm.

(B) Collagen-embedded PAAm bead hydrogel fabrication schematic.

(C) Reflectance (top) and fluorescence (middle) confocal microscopy images of soft PAAm beads embedded within 2.5 mg/mL collagen; scale bar, 100 μm.

(D) Analysis of the local packing fraction of PAAm beads in hydrogels of different component stiffnesses.

(E) 3D reconstruction of granular hydrogel bead packing; scale bar, 50 μm.

(F) Bicinchoninic acid assay analysis of type I collagen concentration (mean ± SD) in beadless and bead-embedded hydrogels. Significance is denoted via compact letter display whereby groups with distinct letters are statistically different from each other ($p < 0.05$). Intensity and contrast of figure micrographs have been altered for visualization purposes.

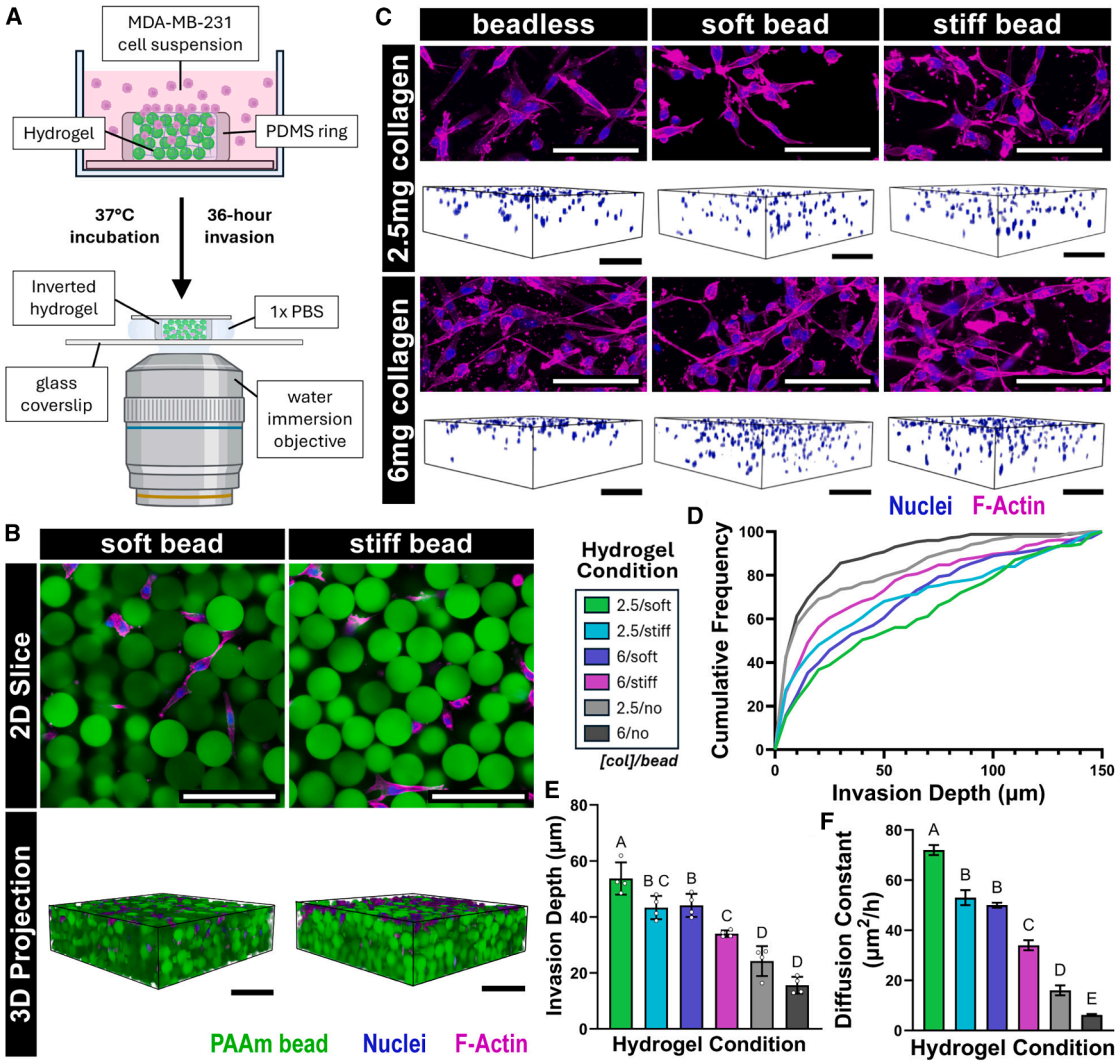


**Figure 3. PAAm beads promote cancer cell invasion through collagen in a stiffness-dependent manner**

(A) Schematic of MDA-MB-231 cancer cell invasion assay experimental setup.

(B) Confocal micrographs of bead-laden 6 mg/mL collagen hydrogels seeded with MDA-MB-231 breast cancer cells stained with DAPI (blue) and phalloidin (magenta); scale bar, 100 μm.

(C) Confocal micrograph 150 μm maximum projections (top) and 3D projections (bottom) of MDA-MB-231 cells invading through 2.5 or 6 mg/mL beadless and granular collagen hydrogels; scale bar, 100 μm.

(D and E) (D) Cumulative frequency distribution and (E) mean ± SD of MDA-MB-231 cell invasion depth after 36-h invasion through granular hydrogels of differing stiffness.

(F) Mean ± SD MDA-MB-231 cell diffusion constants. Significance is denoted via compact letter display whereby groups with distinct letters are statistically different from each other ($p < 0.05$). Intensity and contrast of figure micrographs have been altered for visualization purposes.

have other ECM crosslinking mechanisms. Taken together, these findings validate that our model recapitulates many key structural characteristics of adipose tissue and enables control over the packing of adipocyte mimetics within a selectively tunable ECM.

## PAAm beads promote cancer cell invasion through collagen in a stiffness-dependent manner

Next, we assessed how altering bead stiffness and collagen concentration impacts breast cancer cell migration to approximate the mechanical regulation of breast cancer cell invasion by native adipose tissue. To this end, we seeded invasive MDA-MB-231 triple-negative breast cancer cells on the exposed surface of granular hydrogels and assessed their invasion into the hydrogels after 36 h via confocal microscopy (Figure 3A). This experimental configuration mimicked the interactions of single or small clusters of cancer cells with the native stromal interface at the leading edge of a tumor, independent of tumor growth-induced mechanical force such as solid stress or interstitial fluid pressure (IFP).[58] Considering the inherent variability of primary adipocyte

Please cite this article in press as: Knode et al., Adipose-mimetic granular hydrogels uncover biophysical cues driving breast cancer invasion, Cell Biomaterials (2026), https://doi.org/10.1016/j.celbio.2026.100411



CellPress

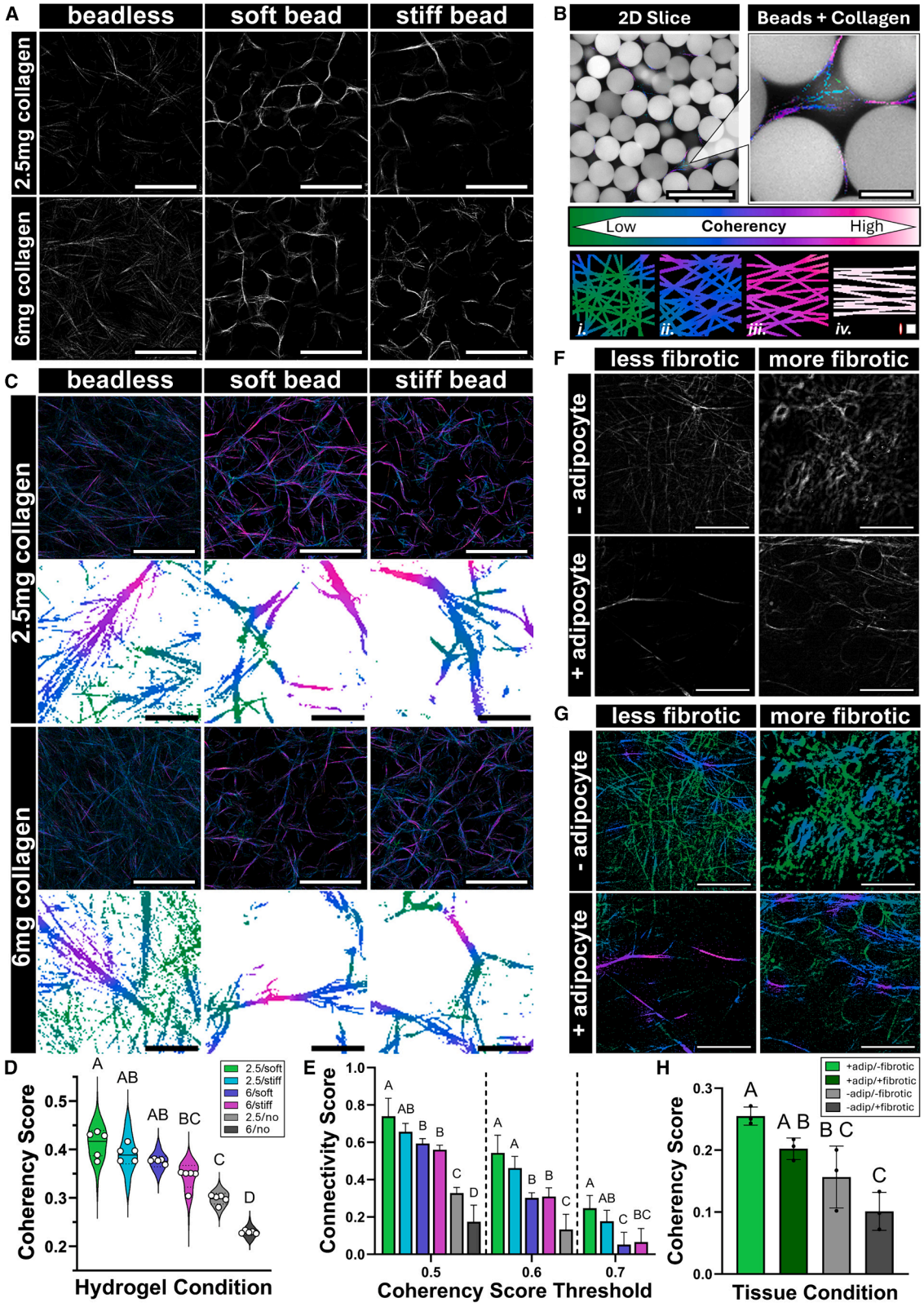


*(legend on next page)*

Please cite this article in press as: Knode et al., Adipose-mimetic granular hydrogels uncover biophysical cues driving breast cancer invasion, Cell Biomaterials (2026), https://doi.org/10.1016/j.celbio.2026.100411



size and stiffness, as well as adipose tissue matrix density, we first conducted a pilot study to identify the parameters that most significantly influence breast cancer cell invasion at early time points. Interestingly, we observed that hydrogel component stiffness (bead or matrix) appears more influential than bead size in coordinating cancer cell migration (Figures S4A and S4B). Cells invaded into the hydrogel in both soft and stiff bead conditions (Figure 3B) and appeared to organize and elongate around PAAm beads. While no significant trends in cell morphology were observed between conditions, the inclusion of either soft or stiff beads significantly increased tumor cell invasion compared with beadless hydrogels (Figure 3C). These findings were highly consistent between experimental replicates (Figure S4C). Additionally, nuclear tracking revealed that MDA-MB-231s invaded the most in 2.5 mg/mL gels with soft beads and the least in 6.0 mg/mL beadless controls, with soft beads facilitating migration compared with stiff or no beads and 2.5 mg/mL collagen facilitating migration compared with 6.0 mg/mL collagen (Figures 3D and 3E). Interestingly, the mean invasion depths of the two intermediate granular hydrogels containing both soft and stiff tissue components (2.5 mg/mL collagen + stiff beads and 6 mg/mL collagen + soft beads) were similar, but the distribution of cell invasion differed between both systems, suggesting concurrent but independent regulation of cell invasion by collagen and beads. These findings were not an artifact of the cell line chosen, as we observed similar trends in a subset of conditions with human MCF10A mammary epithelial cells and murine EO771 hormone receptor-positive breast cancer cells, supporting the broader relevance of our findings (Figures S4D and S4E). Specifically, bead inclusion within the collagen ECM promoted invasion in a stiffness-dependent manner across all cell lines regardless of baseline motility, demonstrating that adipocyte-mimetic bead stiffness and ECM density broadly dictate the migratory activities of mammary cells.

Finally, to better understand the migratory behavior of tumor cells in granular hydrogels, we estimated tumor cell diffusion constants for each condition by plotting the corresponding invasion depth distribution against a half-normal probability distribution, which is known to model diffusive cell motion.[59] We note that cancer cells do not exhibit diffusive behavior at short time scales (e.g., within minutes). We also note cancer cells are not ballistic at long time scales (e.g., within hours), especially when confined by ECM and hydrogel beads. Most likely, the long-time dynamics of the cancer cells in the granular hydrogels can be captured by power-law scaling of the mean-square displacement $(\Delta\vec{r}(t))^2 \sim t^{\alpha}$ with time t, where $1 \leq \alpha \leq 2$, 1 corresponds to diffusive motion, and 2 corresponds to ballistic motion. Quantifying the degree of cancer cell invasion using diffusion (with diffusion constant D) provides a lower bound on how far the cancer cells can invade in a given time, provided the cancer cells are not crowded with sub-diffusive dynamics. Diffusion constants mirrored absolute invasion depth measurements (Figure 3F), though the migratory behavior of cells in stiff bead or beadless conditions was less accurately captured by a diffusive model than cells in soft bead conditions, as indicated by diverging $R^2$ values (Figures S5A and S5B). These findings are not surprising as tumor cells can readily adapt their migratory phenotype under more restrictive conditions and employ mechanisms that are not simply diffusive. For example, with the stiffer beads, the reduced effective free volume would lead to less cancer invasion. Another possible important feature is the collagen in the interstitial regions between beads can become aligned, which can affect the persistence of cancer cell motion. Collectively, our results indicate that the inclusion of PAAm beads facilitates breast cancer cell migration into collagen hydrogels, with the most pronounced effects occurring in low-density collagen hydrogels containing soft beads.

## Inclusion of PAAm beads alters collagen fiber architecture in a concentration-dependent manner

We next sought to characterize how bead incorporation affected collagen network formation, considering its established role in regulating tumor cell migration.[60,61] In native adipose tissue, collagen fibers exhibit linear and aligned geometry between adipocytes,[20] Moreover, it has been shown for other biopolymers that milieu-dependent changes in assembly kinetics influence filament elongation and lateral association.[62] Therefore, we hypothesized that bead incorporation alters collagen fibrillogenesis and anisotropy compared with bead-free collagen. Indeed, confocal reflectance microscopy revealed that inclusion of beads promoted the formation of hierarchical networks of aligned collagen fibers, while beadless hydrogels of both

**Figure 4. Inclusion of PAAm beads alters collagen fiber architecture in a concentration-dependent manner**

(A) 2D slice reflectance micrographs of 2.5 or 6 mg/mL type I collagen in beadless and granular hydrogels; scale bar, 100 μm.

(B) Collagen fiber coherency color survey analysis and representative networks of variable alignment. Scale bars, 100 μm (left), 25 μm (right); focal adhesion scale approximation = 1 × 4 μm (red/white ellipse, bottom right), window size = 3 μm (white square, bottom right).

(C) 40 μm maximum projection reflectance micrographs of 2.5 and 6 mg/mL type I collagen overlaid with a coherency score color survey (top) and a 2D slice raw color survey output (bottom); scale bar, 100 μm (top), 20 μm (bottom).

(D) Violin plots demonstrating average collagen fiber coherency scores depending on hydrogel condition. Significance denoted via compact letter display ($p < 0.05$).

(E) Condition-dependent fiber connectivity analysis (mean ± SD), grouped by coherency score threshold. Statistics were calculated within threshold groups only, and the significance was denoted via compact letter display ($p < 0.05$).

(F and G) (F) Intravital two-photon microscopy of collagen shown by second harmonic generation (SHG), compiled into 5 μm maximum projections capturing varying levels of fibrosis and adipocyte packing in live murine mammary tissue; scale bar, 50 μm; ROIs corresponding to (G). Coherency color survey analysis of 5 μm maximum projection SHG micrographs depicting collagen fiber structure in living murine mammary fat pads imaged via intravital microscopy; scale bar, 50 μm.

(H) Mean ± SD condition-dependent fiber coherency scores for $n = 3$ living murine mammary fat pads. All significance is denoted via compact letter display whereby groups with distinct letters are statistically different from each other ($p < 0.05$). Intensity and contrast of figure micrographs have been altered for visualization purposes.

Please cite this article in press as: Knode et al., Adipose-mimetic granular hydrogels uncover biophysical cues driving breast cancer invasion, Cell Biomaterials (2026), https://doi.org/10.1016/j.celbio.2026.100411



CellPress

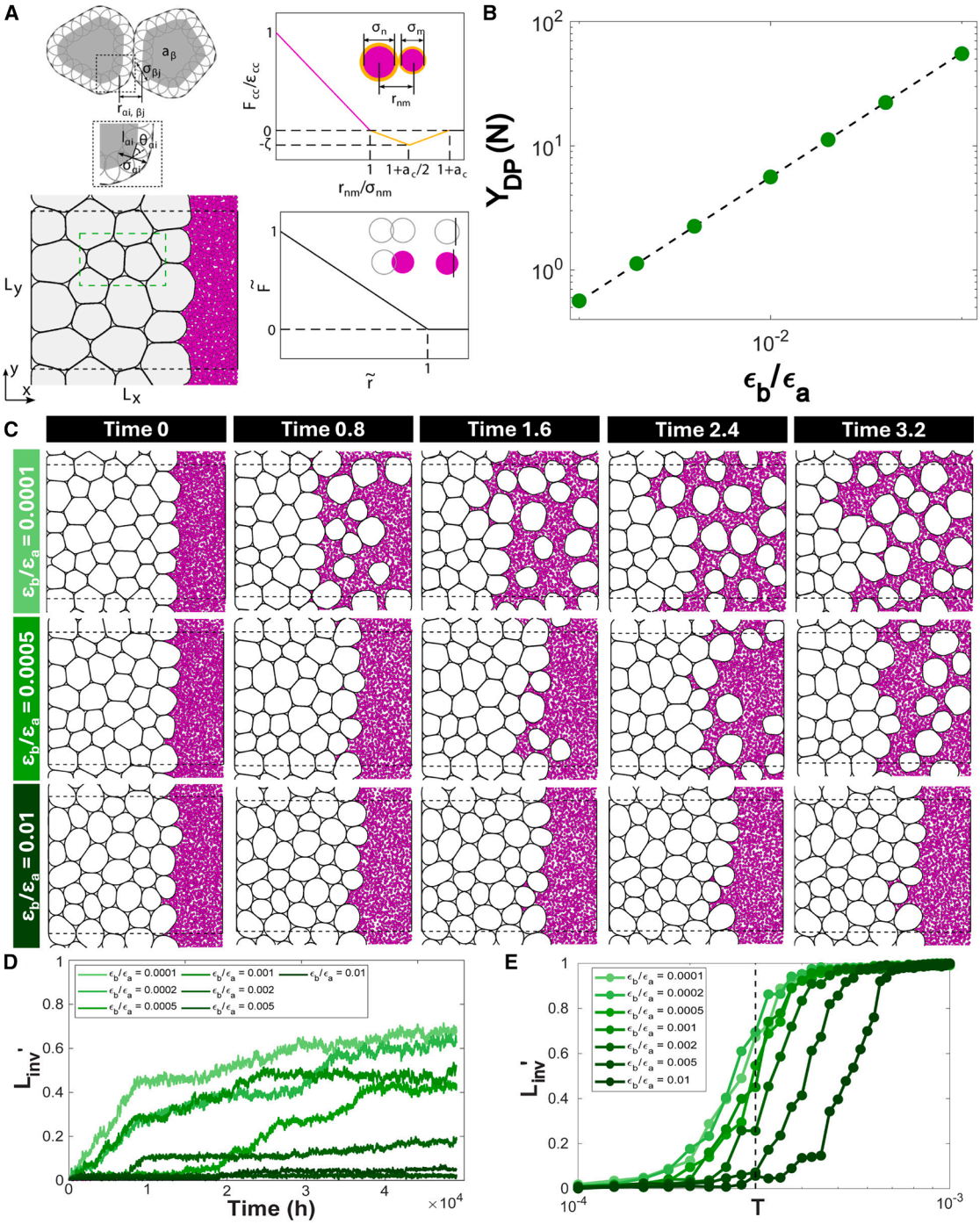


**Figure 5. DEM modeling suggests adipocyte stiffness regulates breast cancer progression**

(A) DEM simulations of breast cancer cell (magenta disks) invasion into packings of adipocytes (gray deformable polygons) in 2D. Adipocytes are modeled as deformable particles (top left panel). Cancer cells are modeled as soft disks with an adhesive shell (top right, where inter-cancer cell forces $F_{cc}$ are calculated as the negative gradient of the potential energy $U_{cc}$). The packings of cancer cells and adipocytes are confined to a rectangular box with periodic boundary conditions in the y-direction and two confining walls at x = 0 and x = $L_x$ (bottom right). A schematic of the purely repulsive force for adipocyte-adipocyte ($\tilde{F} = F_{aa}$, $\tilde{r} = 1 - r_{\alpha i,\beta j}/\sigma_{\alpha i,\beta j}$, overlapping gray disks), adipocyte-cancer ($\tilde{F} = F_{ac}, \tilde{r} = 1 - r_{\alpha i,n}/\sigma_{\alpha i,n}$, overlap between gray and magenta disks), adipocyte-wall ($\tilde{F} = F_{aw}$, $\tilde{r} = 1 - x_{\alpha i}/\sigma_{\alpha i}$ or $1 - (L_x - x_{\alpha i})/\sigma_{\alpha i}$, overlap between gray disk and vertical line), and cancer-wall ($\tilde{F} = F_{aa}, \tilde{r} = 1 - x_n/\sigma_n$ or $1 - (L_x - x_n)/\sigma_n$, overlap between magenta disk and vertical line) interactions is provided in the bottom right panel.

(B) The compressive stiffness of a single adipocyte $Y_{DP}$, versus the bending strength $\varepsilon_b$, normalized by $\varepsilon_a$, using the deformable particle model.

*(legend continued on next page)*

Please cite this article in press as: Knode et al., Adipose-mimetic granular hydrogels uncover biophysical cues driving breast cancer invasion, Cell Biomaterials (2026), https://doi.org/10.1016/j.celbio.2026.100411



collagen densities lacked this organization (Figure 4A). Collagen fibers were also slightly thinner in beadless conditions, and there were no appreciable differences in fiber length or fiber straightness (Figure S6A). To quantify potential differences in fiber alignment more rigorously, we used the open-source Fiji plugin OrientationJ,[63] which can assign each collagen fiber in an image a coherency score based on its relative alignment to nearby fibers (Figure 4B). Notably, collagen fibers in hydrogels with PAAm beads were significantly more coherent, or anisotropic at a locally defined scale, than fibers in beadless hydrogels (Figure 4C) with high consistency between experimental replicates (Figure S6B). Of note, 2.5 mg/mL hydrogels demonstrated a higher fraction of aligned collagen fibers compared with 6.0 mg/mL hydrogels, regardless of whether PAAm beads were included (Figures 4D and S6C). Although bead stiffness did not affect fiber coherency between collagen density-matched granular hydrogels, we observed a trend suggesting an inverse relationship between bead stiffness and average fiber alignment (Figure 4D). As further proof of concept, we quantified the eccentricity of individual collagen fibers computationally[64] and observed similar trends whereby fiber eccentricity increased upon bead integration compared with beadless controls (Figures S6D and S6E). Moreover, considering the preferential migration of cells along highly aligned ECM structures,[60] we aimed to assess the 3D interconnectivity of collagen fibers as a function of fiber alignment. To this end, we employed a custom image analysis workflow, which allowed us to isolate grouped collagen fibers in accordance with an increasingly stringent coherency threshold (Figure S6F). This analysis yielded volumetric and raw count data for both the complete collagen network as well as smaller, interconnected collagen networks identified above a certain coherency threshold. These data were then used to define a ''connectivity'' term describing the thresholded collagen network volume as a fraction of the total unthresholded collagen network volume (Figure 4E). We found that the collagen fibers in granular hydrogels were significantly more interconnected than those of beadless gels across all coherency scores, which surpassed the percolation threshold (Figure 4E). At higher coherency thresholds, granular hydrogels similarly demonstrated increased fiber interconnectivity when fabricated with 2.5 mg/mL collagen compared with 6.0 mg/mL collagen, suggesting that the hierarchical structure of collagen networks is coordinated by bead inclusion and is dependent on local ECM density. Collectively, our results indicate that the inclusion of PAAm beads coordinates collagen fiber architecture in granular hydrogels, yielding more aligned and interconnected fibers relative to beadless controls, an effect that is more pronounced at lower collagen densities.

To validate the *in vivo* relevance of these findings, we employed high-resolution multiphoton imaging techniques on the mammary fat pads of live mice.[65,66] SHG (collagen) images depicting tissue regions varying in levels of collagen fibrosis and local adipocyte packing were acquired (Figures 4F and S7A). Comparing the ratios of positive (collagen signal) to negative (background) pixel values between conditions demonstrated differing degrees of fibrosis represented by the image stacks selected for analysis (Figure S7B). Next, to compare relative levels of fiber alignment dependent on adipocyte presence and fibrosis, these image stacks were subjected to the same OrientationJ color survey workflow as the *in vitro* image sets (Figures 4G and S7C). Mirroring the trends demonstrated by the granular hydrogels, adipocyte packing appeared to coordinate fiber architecture compared with paired tissue regions absent of adipocytes, and fiber alignment significantly increased around adipocytes in both fibrotic and nonfibrotic conditions, corresponding to larger bulk tissue coherency scores (Figure 4H). We note that raw coherency scores differ greatly between *in vitro* and *in vivo* data and attribute this variability to differences in image acquisition parameters such as objective magnification and step size, characteristically poor intravital resolution due to light scattering, and the presence of other tissue structures such as vasculature. Interestingly, however, the coherency scores of fibrotic conditions appeared to change more drastically in the presence of adipocytes compared with less fibrotic tissue regions, again paralleling the trends demonstrated in the granular hydrogels (Figure S7D).

## DEM modeling suggests adipocyte stiffness regulates breast cancer progression

We observed that breast cancer cell invasion increased in soft bead hydrogels compared with stiff bead hydrogels, regardless of collagen concentration, and that collagen fiber alignment did not significantly differ with bead stiffness. Hence, differences in collagen architecture alone cannot explain bead stiffness-dependent differences in breast cancer cell invasion. To explore the effect of adipocyte-like bead stiffness on breast cancer cell invasion *in silico*, we employed discrete element method (DEM) simulations of adipose tissue. First, we varied the stiffness of the adipocytes via the bending strength $\varepsilon_b$ to study the impact of adipocyte stiffness on breast cancer invasion. We found that the compressive stiffness of a single adipocyte increases linearly with $\varepsilon_b$ (Figure 5B). Next, in typical simulations of breast cancer invasion into adipose tissue, we found that the degree of invasion $L'_{inv}$ increases over time and then reaches a plateau at long time points, as shown in Figures 5C and 5D. The long-time plateau in $L'_{inv}$ increases with increasing mean speed or activity as parameterized by T (Figure 5D), in agreement with experimental observations that more motile cancer cells are more invasive. Furthermore, we found that stiffer adipocytes give rise to reduced cancer cell invasion. In particular, we show that the degree of invasion $L'_{inv}$ is smaller for adipocytes with larger $\varepsilon_b$ when the cancer cells have the same thermal activity (Figure 5D). This result suggests that cancer cells must be more motile to achieve the same $L'_{inv}$ with stiffer adipocytes compared with softer adipocytes (Figure 5E). The observation of hindered cancer invasion into adipose tissue with increased adipocyte stiffness is

(C) Examples of packings of cancer cells and adipocytes with different bending energies $\varepsilon_b/\varepsilon_a$ at different times ($\times 10^4$ h) during invasion.
(D) Rescaled invasion degree $L'_{inv}$ plotted versus time for various $\varepsilon_b/\varepsilon_a$ indicated by the colors.
(E) The invasion degree $L'_{inv}$ at long times plotted versus the cancer cell temperature T for various $\varepsilon_b/\varepsilon_a$ indicated by the colors. Three different configurations are used for the average for each $\varepsilon_b/\varepsilon_a$.

Please cite this article in press as: Knode et al., Adipose-mimetic granular hydrogels uncover biophysical cues driving breast cancer invasion, Cell Biomaterials (2026), https://doi.org/10.1016/j.celbio.2026.100411



CellPress

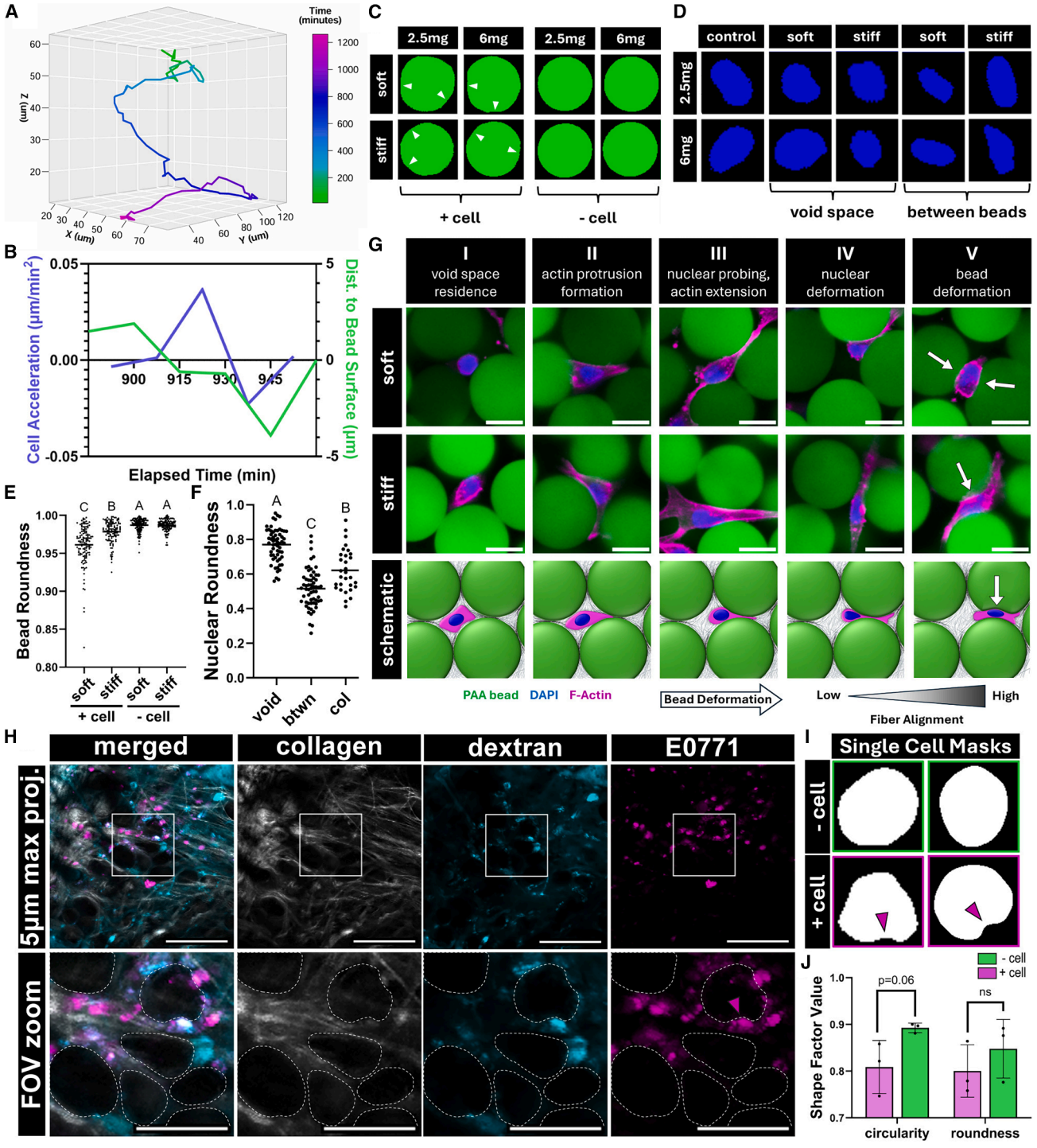


**Figure 6. PAAm bead-induced cell nuclear deformation and local packing geometry influence breast cancer cell invasion**

(A) Plot of a single tracked nucleus migrating through a soft bead of 2.5 mg/mL granular hydrogel imaged over 21 h via spinning disk confocal microscopy.

(B) Plot depicting a moment of nuclear acceleration (left axis, blue) correlating with a reduction in nearest bead proximity (right axis, green) as a single cell squeezes between two beads.

(C) Segmented masks of 2.5 or 6 mg/mL granular hydrogel bead deformation with or without cell contact.

(D) Segmented cell masks of nuclear deformation for cells residing in the void or interstitial spaces between beads in 2.5 or 6 mg/mL granular hydrogels.

(E) Plot of soft and stiff PAAm bead deformation, collected from both 2.5 and 6 mg/mL granular hydrogels, evaluated via roundness shape parameter. Significance is denoted via compact letter display whereby groups with distinct letters are statistically different from each other ($p < 0.05$).

*(legend continued on next page)*

Please cite this article in press as: Knode et al., Adipose-mimetic granular hydrogels uncover biophysical cues driving breast cancer invasion, Cell Biomaterials (2026), https://doi.org/10.1016/j.celbio.2026.100411



consistent with the experimental results in our experimental model. We note that the predicted timescale for full invasion of the cancer cells into adipose tissue is much longer compared with that found in experiments (less than 2 days). This difference can be attributed to the fact that we use the typical invasion speed of cancer cells in isolation in this model,[67] and future intravital time course studies should be conducted to better characterize the velocity of cancer cells *in vivo*.

### PAAm bead-induced cell nuclear deformation and local packing geometry influence breast cancer cell invasion

Physical constraints regulate tumor cell invasion due, in part, to the rate-limiting process of nuclear deformation during confined migration.[68,69] To assess how the organization and confined packing of PAAm beads impacted migration dynamics in our system, we tracked the trajectories of invading MDA-MB-231 breast cancer cells through the most mechanically permissive granular hydrogel condition (2.5 mg/mL collagen + soft beads) (Figure 6A). While cancer cell migration speeds fluctuated significantly over the invasion period, no generalizable correlation between cell speed and bead proximity was discernible. However, when tracking only the most motile cells, we observed that these subpopulations stalled, rapidly accelerated, and then decelerated as they squeezed between adjacent beads (Figures 6B and S8A). This pattern is consistent with previous studies of confined migration, which showed that tumor cells produce cytoskeletal protrusions to pull themselves through confining spaces,[70,71] consequentially deforming their nuclei and generating additional forces through a recoil mechanism, before returning to slower migration speeds.[72] In line with this model, we observed both bead (Figure 6C) and nuclear deformation (Figure 6D) when migrating tumor cells were in direct contact with the adipocyte-mimetic PAAm beads. Specifically, both soft and stiff beads were significantly deformed at the cell contact interface compared with those uncontacted by cells (Figure 6E). Similarly, nuclei localized in unconfined void spaces between beads were significantly rounder than nuclei between bead-bead interfaces, while nuclei in beadless hydrogels adopted an intermediate phenotype (Figure 6F). Moreover, tumor cells were able to deform soft beads significantly more than stiff beads, consistent with a less physically restrictive environment and the greater cell invasion depths we observed in soft granular hydrogels. Interestingly, we did not detect differences in bead deformation between 2.5 and 6.0 mg/mL granular hydrogels (Figure S8B), highlighting the need to consider the mechanics of other tissue features besides the ECM. Likewise, we did not observe consistent differences in nuclear deformation across mechanical conditions (Figure S8C), indicating that nuclear stiffness may be a limiting factor in the migration trajectories we measured. Taken together, these data suggest that both tumor cell intrinsic (e.g., nuclear[68,69,73] or cell stiffness[74,75]) and extrinsic (bead/adipocyte) mechanics influence the migratory behavior of breast cancer cells in a dynamic, multi-step manner (Figure 6G).

To determine how invasive tumor cells affect adipocyte morphology *in vivo*, intravital images of murine mammary fat pads were acquired 2 weeks after being orthotopically injected with syngeneic EO771-YFP (yellow fluorescent protein) cancer cells. By co-registering images of cancer cells with high-contrast images of surrounding collagen (SHG) and blood plasma (fluorescent dextran), we manually identified adipocytes that did or did not contribute to the confinement of invading EO771 cells (Figure 6H; see methods for selection criteria). Consistent with our *in vitro* observations, cancer cell confinement between adipocytes correlated with adipocyte deformation (Figure 6I). Quantification of adipocyte shape via image analysis confirmed that adipocytes in direct contact with EO771 cells were less circular and round as compared with adipocytes not in contact with tumor cells (Figure 6J). Adipocytes in contact with relatively unconfined cancer cells also exhibited some level of deformation, but not to a comparable degree (Figure 6I). The parallels between these *in vivo* findings and our *in vitro* data collected from the granular hydrogels suggest that mechanical interactions between cancer cells and adipocytes may play a role in tumor dissemination through the adipocyte-rich mammary stroma.

## DISCUSSION

We developed mechanically tunable granular hydrogels that mimic structural features of adipose tissue and demonstrated the utility of this model for studying the physical regulation of breast cancer invasion. More specifically, we fabricated murine adipocyte-sized PAAm beads[41,42] that recapitulated the stiffness of either soft or stiff adipocytes. We incorporated these beads into 3D collagen hydrogels of varying density to replicate the physical constraints that breast cancer cells experience as they invade between mammary adipocytes and their surrounding ECM.[5,11,12] Interestingly, breast cancer cells invaded bead-containing 3D collagen gels more readily than bead-free controls, regardless of bead stiffness and collagen density; however, this effect was greatest under compliant local mechanical conditions (i.e., soft beads and reduced collagen density). Consistent

(F) Plot of nuclear deformation data, collected from both 2.5 and 6 mg/mL collagen hydrogels, describing the localization of a nucleus to unconfined void regions ("void") or confined regions between ("btwn") soft or stiff PAAm beads in granular hydrogels, or in beadless collagen ("col") hydrogels, evaluated via roundness shape parameter. Significance denoted via compact letter display ($p < 0.05$).

(G) Schematic depicting migratory mechanisms of single cells invading between adipocyte-mimetic beads with corresponding micrographs captured in 2.5 mg/mL collagen granular hydrogels; scale bar, 25 μm.

(H) Intravital micrographs compressed into 5 μm maximum projections of SHG (collagen) and fluorescent (separate dextran and E0771) signal, depicting breast cancer cells (magenta) migrating between and deforming adipocytes (gray outline) in living murine mammary tissue; scale bar, 50 μm (top), 25 μm (bottom); arrows indicate E0771 contact deformation.

(I) Manually interpolated single-slice cell masks of live mammary tissue-resident adipocytes, with representative single-cell masks depicting cancer cell-deformed (pink/bottom) and undeformed (green/top) adipocyte cross-sections, and arrows indicate E0771 contact deformation.

(J) Graph depicting differences (mean ± SD) in adipocyte cross-section roundness and circularity depending on E0771 cell contact in $n = 3$ living murine mammary fat pads, statistics denoted in bracket format ($p < 0.05$). Intensity and contrast of figure micrographs have been altered for visualization purposes.

Please cite this article in press as: Knode et al., Adipose-mimetic granular hydrogels uncover biophysical cues driving breast cancer invasion, Cell Biomaterials (2026), https://doi.org/10.1016/j.celbio.2026.100411



with previous findings that collagen fiber alignment promotes directional cell migration,[21,60,61,76] we found that collagen fibers in bead-containing hydrogels were more aligned and interconnected, likely contributing to our results. Nevertheless, increased deformation of compliant beads by confined migratory cancer cells was similarly important in line with previous work showing that physical confinement regulates cancer cell malignancy[77,78] and migration speed.[22,70,72] Indeed, our DEM model of breast cancer-seeded adipose tissue also demonstrated that more compliant adipocytes promote cancer cell invasion, and *in vivo* experiments revealed instances of adipocyte deformation by confined migratory cancer cells. Taken together, our data suggest that adipose tissue microarchitecture and local mechanical anisotropy are likely to influence breast cancer invasion through the mammary stroma within.

Interestingly, cells invading through soft bead granular hydrogels demonstrated a more diffusive phenotype compared with stiff bead granular hydrogels and beadless controls, both of which promoted cell invasion patterns that could not be attributed to diffusion alone. While not directly validated *in vivo*, these data suggest that adipocyte structure promotes cancer cell migration by altering the physical tumor microenvironment and that cells navigating between stiffer adipocytes must adopt a more active (less diffusive) phenotype. Indeed, previous studies have found that stiffer tissue components can force invasive tumor cells to mechanically adapt to their local microenvironment, as tissue organization[79] and decreased 3D substrate stiffness[80,81] promote cell migration and select for aggressive metastatic phenotypes.[82] Further, given that the simple diffusive model for cancer cell motion in collagen hydrogel mixtures only estimates baseline activity dependent on bead properties, our results highlight the need for future studies to evaluate correlations between collagen fiber orientation, density, and cancer cell motion.

To this point, our analyses highlighted an ECM density-dependent increase in local fiber alignment and hierarchical network structure in granular hydrogels compared with beadless controls. In line with these findings, several previous studies have highlighted how macromolecular crowding[83,84] and local ECM properties (density, degree of crosslinking)[85] can alter the self-assembly and 3D architecture of collagen networks by limiting the dimensionality of collagen fibril nucleation. Validating these trends *in vivo*, intravital imaging of EO771 breast cancer-seeded murine mammary fat pads revealed similar patterns, and tissue regions with ranging degrees of fibrosis demonstrated increased collagen fiber organization when packed with adipocytes. This kind of local ECM anisotropy is known to play a large role in the directional contact guidance of migratory cells,[21,60,61] and aligned collagen fibers orient migratory cell protrusions,[86] drive traction force-mediated cell movement,[87] and increase the persistence of invasive cells.[60] Given the significant increase in both fiber organization and cell invasion in our granular hydrogels compared with beadless controls and qualitative observations of interstitial collagen-aligned cell protrusions through bead-bead interfaces (Figure 6G), it is possible that observed cell invasion phenotypes can be attributed, at least in part, to bead-coordinated differences in fiber structure. Finally, we observed no mechanically coordinated differences in the nuclear shape factor of migrating cells, indicating that adipocyte mechanics do not inherently alter nuclear deformability. PAAm beads in direct contact with cells, however, demonstrated significant stiffness-dependent differences in deformation, which corresponded with moments of nuclear acceleration and deceleration as migratory cells squeezed between beads. Cell nuclei, which are traditionally considered to be the stiffest organelle,[88] are known to act as a rate-limiting factor in confined cell migration in order to prevent DNA damage.[68,69,89] Within this context, our data suggest that as breast cancer cells migrate between adipocytes during invasion, adipocyte stiffness-coordinated confinement of migratory nuclei dictates the velocities of the tumor cell. These data also mirror the findings of other studies, which suggest that some degree of nuclear confinement temporarily alters cell migration through a force-generating recoil mechanism.[72] We therefore hypothesize that the mechanical properties of stiff adipose tissue, while restrictive of diffusive cell movement, may further coordinate the migration of invasive cancer cells by promoting such moments of nuclear recoil. Interestingly, other recent publications highlight traction force-mediated differences in cell migration in response to varying levels of local confinement, and migratory cells seem to generate polarized traction forces with increased substrate (ECM) stiffness and nuclear confinement, leading to differences in nuclear deformation and migration phenotype that are mediated by cytoskeletal machinery.[90,91] This mechanism results in a biphasic cell velocity trend whereby soft/unconfined and stiff/confined microenvironments may both promote invasion by regulating this traction force generation/nuclear deformation axis, further supporting the theory that matrix structure and PAAm bead stiffness play tandem roles in regulating breast cancer invasion though granular hydrogels.

While the intravital data presented in this report did not have the resolution to evaluate deformation patterns in invasive cell nuclei, we were able to visualize the reciprocal deformation demonstrated by confinement-inducing adipocytes. Thus, to validate these reciprocal cell-bead deformation patterns *in vivo*, the shape factors of individual adipocyte cross-sections that were or were not contributing to the confinement of cancer cells were compared. This analysis yielded similar results as our *in vitro* experiments, demonstrating increased deformation of adipocytes contributing to cancer cell confinement, and further suggesting that adipocyte packing in mammary tissue physically regulates the invasive activity of breast cancer. Additional studies will be needed to explore this hypothesis and elucidate whether additional tumor cell mechanical characteristics influence adipose tissue invasion, especially considering the recent demonstration of how breast tumor cell viscosity dictates interactions with the vasculature in downstream metastatic processes.[92]

Given our findings using PAAm beads as adipocyte mimetics, we propose the following theoretical model of breast cancer cell invasion through adipose tissue (Figure 6G). First, a given tumor cell resides within a less confined void space of the tissue (I), followed by the formation of actin-rich protrusions that extend along the dominant axis of collagen fiber alignment between adjacent adipocytes (II). These protrusions extend beyond this region of peak confinement and then begin to pull the tumor

Please cite this article in press as: Knode et al., Adipose-mimetic granular hydrogels uncover biophysical cues driving breast cancer invasion, Cell Biomaterials (2026), https://doi.org/10.1016/j.celbio.2026.100411



cell through the interstitial space between adipocytes, with the nucleus acting as a mechanical probe limiting migration (III). The migrating nucleus begins to deform, generating recoil force until it achieves a certain threshold at which it can no longer be compressed without risk of DNA damage due to confinement-induced chromatin remodeling (IV), which could ultimately lead to adaptive differences in tumor cell aggression. Finally, the tumor cell rapidly passes between the adipocytes, which reciprocally deform in response to transmigration (V).

This theoretical model offers insight into the cell-scale mechanical regulation of invasive cancer cells by native stromal adipocytes, emphasizing the migration-facilitating alignment of collagen fibers parallel to bead (adipocyte) interfaces and the rate-limiting, stromal stiffness-dependent confinement of migrating cells. The model is also consistent with findings of many previous studies, which describe the morphological plasticity migratory cells adapt as they encounter physically restrictive stromal structures or anisotropic ECM substrates,[70,93–95] as well as the unique rate-limiting but force-generating properties of confined cell nuclei.[68,69,72] Future validation of the model could be achieved by perturbing the ability of migratory cells to form traction-generating cytoskeletal protrusions,[95,96] as well as disrupting the structural integrity of the nuclear envelope.[97] Moreover, additional intravital imaging of other breast cancer cells migrating through native murine mammary adipose[98,99] is needed to confirm the broad relevance of our findings, with the added potential to inform clinical prognostic imaging techniques in the future.

Like all model systems, adipose-mimetic granular hydrogels present some biological and technical limitations. For example, we used consistently sized particles to limit the confounding effects of varied bead curvature in polydisperse systems[100] that can affect collagen fibrillogenesis and migration independently.[23,101] As native adipocyte size is heterogeneous, future studies with mixtures of differently sized PAAm particles will gain further insights into how adipocyte size and its heterogeneity affect our findings. Interestingly, a recently published study employing a biphasic hydrogel system suggests that ovarian cancer invasion mode is regulated by particle size and volume fraction, further demonstrating the importance of adipose tissue structure in regulating cancer progression.[39] Moreover, adipocytes are known to express adhesion molecules in order to bind to the surrounding matrix and maintain tissue structure. While the system described here is artificially supported by a PDMS microwell during hydrogel polymerization and tissue culture, our rheology data make it clear that the bulk mechanical properties of granular hydrogels differ from those of adipose tissue in the absence of these adhesive molecules. To better recapitulate these features in the future, it may be necessary to functionalize the surface of PAAm beads with adhesion ligands, such as poly-L-lysine[42] or collagen-binding motifs, to better recapitulate adipocyte-ECM interactions. Additionally, PAAm gels tend to be highly elastic, while adipocytes also demonstrate viscoelastic properties.[102] Future iterations of this model system could alter the viscoelastic properties of adipocyte-like beads by fabricating them from PAAm with linear polymer chains to alter viscoelasticity[103] or mixtures with other viscoelastic polymers such as alginate.[104] Lastly, due to the light-scattering properties of PAAm, imaging resolution through these granular hydrogels deteriorates as acquisition depth increases, restricting the hydrogel size as well as the cell culture period over which imaging is possible. Here, we cast granular hydrogels into micron-sized PDMS molds to overcome these limitations while excluding artifacts caused by limited transport of oxygen and other canonical morphogens.[105]

Finally, while our model lacks other relevant stromal cell populations, ECM components, and adipokines secreted by native adipocytes, our platform lends itself to incorporating these factors directly into the collagen matrix or the culture media. Some granular hydrogel systems have been leveraged to study other cell types and have, for example, demonstrated how cancer cell phenotype and matrix composition coordinate adipose-derived stromal cell (ADSC) transition into cancer-associated fibroblasts (CAFs).[38] In the future it will also be important to evaluate the biochemical consequences of these granular hydrogels, such as the mechanical regulation of cell-induced proteolytic ECM remodeling, which is known to play a significant role in confined cell migration through fibrotic ECM.[106–108] Interestingly, a recent granular hydrogel study demonstrated MMP (matrix metalloproteinase)-independent migration along microparticle-ECM interfaces, further suggesting that the unique microarchitecture of adipose tissue plays a role in dictating biochemical phenotypes of invading cancer cells.[39] While it is clear that mechanical cues inform cell migration speed and phenotype, resulting biochemical processes must be investigated to fully understand these mechanical mechanisms. Regardless, insights gathered from our system could inform future studies into the mechanical regulation of solid tumors arising in adipose-rich stroma (skin, ovarian, prostate, etc.)[109] and have the potential to make a clinical impact by informing prognostic and diagnostic criteria across cancer types. Ultimately, our analyses highlight the impact of adipocyte and ECM mechanics on tumor cell invasion and demonstrate the need to further elucidate the mechanisms by which adipose stroma regulates breast cancer invasion.

## METHODS

### Murine adipose tissue harvest and histology

For animal studies, 28,000 ES272 cells were injected into the ducts of the fourth mammary glands of female C57BL/6 mice (The Jackson Laboratories) bilaterally. ES272 cells are a syngeneic C57BL/6 breast cancer cell line with constitutively active and mutated PI3KCA (H1047R) (gifted from Dr. Ramon Parsons, Mount Sinai). 11 days post injection, animals had reached humane endpoints. Animals were weighed, and final tumor volumes were measured with calipers. Mice were euthanized via $CO_2$ inhalation, and then resected adipose tissue and mammary tumors were fixed in 4% (w/v) paraformaldehyde (PFA) in 1× PBS for 18 h at 4°C. Resected tumors were then stored in 70% (v/v) ethanol in water at 4°C until processing. Samples were sent to the Cornell College of Veterinary Medicine Animal Health Diagnostic Center for paraffin embedding, sectioning, and staining with hematoxylin and eosin or Masson's trichrome. Stained sections were imaged and digitized on an Aperio ScanScope CS2 (Leica) with a 40× objective. All animal

Please cite this article in press as: Knode et al., Adipose-mimetic granular hydrogels uncover biophysical cues driving breast cancer invasion, Cell Biomaterials (2026), https://doi.org/10.1016/j.celbio.2026.100411



protocols (2009-0117 and 2011-0006) were approved by the Institutional Animal Care and Use Committees at Weill Cornell Medicine and Cornell University.

### Primary adipocyte isolation

Subcutaneous adipose tissue was collected from male C57BL/6 mice (The Jackson Laboratories) at 14 weeks of age after 6 weeks of a high-fat diet (Research Diets, cat# D12330) fed *ad libitum*.[110] Primary adipocytes were then isolated from resected adipose tissue as previously described.[43] Briefly, adipose tissue was minced for several minutes until separated into ~1 $mm^3$ pieces in Krebs-Ringer HEPES buffer (116 mM NaCl, 25 mM HEPES, 4 mM KCl, 2 mM D-glucose, 1.8 mM $CaCl_2$, 1 mM $MgCl_2$) supplemented with 1% (w/v) BSA (KRHB). Floating tissue pieces were then digested in 1.5 mg/mL collagenase type I (Worthington Biochemical #LS004197) in Hank's Buffered Salt Solution (Gibco #14065056) supplemented with 1% (w/v) BSA for 50 min at 37°C. The resulting cell suspension was passed through 200 μm cell strainers (pluriSelect #435020003) to remove undigested pieces of tissue. Adipocytes were allowed to float out of solution for 10 min before the infranatant was aspirated and fresh KRHB was added. This process was repeated three times to enrich for adipocytes and remove contaminating stromal vascular cells.

### Tunable PAAm bead fabrication

Alexa Fluor 488-labeled PAAm beads were produced and analyzed as previously described.[41,42] Briefly, a PDMS-based microfluidic chip employing a flow-focusing geometry was utilized to produce PAAm pre-gel droplets. The chip design incorporates two inlets for the PAAm pre-gel mixture and oil flows and one outlet for droplet collection. The chip features a cross-junction with a width of 40 μm, which gradually widens downstream to 50, 100, and 150 μm, while maintaining a constant channel height of 60 μm.

The PAAm pre-gel droplets were produced in fluorinated oil (3M Novec 7500, Iolitec Ionic Liquids Technologies) containing ammonium Krytox surfactant (2.4%w/v) as an emulsion stabilizer, N, N, N′, N′-tetramethylethylenediamine (TEMED) (0.4% v/v) (Sigma-Aldrich) as a catalyst, and acrylic acid N-hydroxysuccinimide ester (NHS) (0.1% w/v) (Sigma-Aldrich) to include NHS functional groups into the final gel meshwork for binding of Alexa Fluor 488 hydrazide. The pre-gel mixture contained acrylamide (40% w/v) (Sigma-Aldrich) as a monomer, bis-acrylamide (2% w/v) (Sigma-Aldrich) as a crosslinker, ammonium persulphate (0.05% w/v) (Sigma-Aldrich) as a radical initiator, and Alexa Fluor 488 hydrazide (2 mg/mL) (Thermo Fisher) diluted in 10 mM Tris buffer (pH = 7.48). Total monomer concentration in the pre-gel mixture together with the droplet diameter was fine-tuned to obtain beads with well-defined diameter and elasticity. After in-drop polymerization, the beads were washed and resuspended in 1× PBS (pH = 7.4). The diameter of the beads in PBS was analyzed by acquiring bright-field images of the beads (Zeiss AxioObserver.A1, A-Plan 10×/0.25 objective) and by analyzing them using a macro implemented on open-source Fiji. Elasticity was measured by AFM indentation.

### AFM

Isolated adipocytes were immobilized to glass-bottom Petri dishes (World Precision Instruments #FD35100) pre-coated with 5 μg/$cm^2$ Cell-Tak Cell and Tissue Adhesive (Corning #354240) per manufacturer's instructions. In short, freshly isolated primary adipocytes were tightly packed by aspirating infranatant buffer and supernatant-free lipid as previously described,[43] then pipetted directly onto the prepared Cell-Tak substrate. Adipocytes were maintained in a 37°C incubation chamber and allowed to attach for several minutes before being submerged in imaging media. A subset of the sample was stained with Hoechst prior to AFM to confirm that the isolated structures were true adipocytes, rather than residual lipid droplets (Figure S1B). For AFM indentation experiments on adipocytes and PAA beads, a Nanowizard IV was used (JPK BioAFM, Bruker Nano). PNP-TR-TL-Au (Pyrex-Nitride Probe - Triangular - Tipless - Gold) cantilevers (NanoWorld) with a nominal spring constant of 0.32 N/m were employed. These probes have been previously modified with a polystyrene bead of 5 μm diameter (microparticles) and calibrated by the thermal noise method on the surface of a glass slide with milliQ water. The measurements were performed directly in the Petri dishes on the surface of which adipocytes or PAA beads were immobilized as described above. A maximum force load of 15 nN at a rate of 5 μm/s in z closed-loop feedback mode was used. AFM force-indentation analysis was performed using the open-source analysis software PyJibe (GitHub Repository: https://github.com/afm-analysis/pyjibe; version 0.14.0). The Poisson's ratio was set to 0.5 for all analyses. We applied the Hertz/Sneddon model for a spherical indenter with a limitation of the indentation curve to 1.5 μm from the contact point. A geometrical correction factor (k) was applied to correct the indentation for the additional deformation of the spherical shape coming from the substrate.[111] The correction factor $k$ was calculated using

$$k = \frac{\sqrt[3]{R_s}}{\sqrt[3]{R_s} + \sqrt[3]{R_{eff}}},$$

where $R_s$ is the sample radius, and the effective radius ($R_{eff}$) is given by

$$R_{eff} = \frac{R_i R_s}{R_i + R_s},$$

where $R_i$ is the indenter radius. Further details of this procedure can be found in the documentation for Nanite (Python Library: https://nanite.readthedocs.io/en/stable/sec_fitting_guide.html#geometrical-correction-factor).

### SHG imaging

Multiphoton imaging was performed on rehydrated paraffin-embedded slices of human breast adipose tissue, as well as excised mammary fat pad tissue from a 10-week-old C57BL/6J mouse, using an inverted Zeiss 880 confocal/multiphoton laser scanning microscope. Imaging was performed with non-descanned detection, 900 nm excitation, and a Zeiss C-Achroplan 32×/0.85 W Corr M27 objective. Emitted light was filtered for SHG (360–405 nm) to visualize collagen fibers.

## Microwell fabrication

Customizable PDMS microwells were constructed using the Sylgard 184 Silicone Elastomer Kit (Dow #000000818156), and PDMS was selected as the material of choice due to its versatility and well-documented biocompatibility with proper preparation.[112–114] Reagents A (polymer base) and B (curing agent) were combined at a 10:1 ratio, respectively, and vigorously mixed for 5 min. This mixture was transferred to a 150 mm diameter polystyrene Petri dish, degassed for 10 min in a vacuum chamber, and cured overnight at 60°C. Once cooled, microwells were cut from the cured PDMS using Integra Miltex 4 mm (inner well diameter), 8 mm (outer well diameter), and 10 mm (lid) disposable biopsy punches and stored in a 100 mm diameter Petri dish. The PDMS lids were submerged in 70% (v/v) ethanol in water, vigorously shaken on a rocker for 20 min, and allowed to air dry under sterile conditions. Single 18 mm round #1 cover glasses (VWR #16004-300) were similarly washed and dried, then placed in the wells of a 12-well cell culture plate (Falcon #351143). The 12-well plate and microwell-containing Petri dish were plasma treated (Harrick Plasma) on the highest setting for 1 min. Microwells were then transferred to the 12-well plate and bonded to the glass coverslips via an additional 5-min round of air plasma treatment. For live cell tracking experiments, PDMS microwells were bonded to glass-bottomed culture dishes (VWR #10810-054) rather than circular coverslips. Microwell surfaces were lastly treated with 1% (v/v) poly-ethylenimine (PEI, Sigma-Aldrich #181978) for 10 min, 0.1% (v/v) glutaraldehyde (Sigma-Aldrich #G7651) for 30 min, thoroughly rinsed with sterile water, and stored at 4°C.

## Hydrogel preparation

To fabricate the hydrogels, collagen-bead mixtures were prepared over ice and cast into chilled PDMS microwells. Rat tail collagen I (Corning #354249) was selected due to its thoroughly characterized self-assembly into fibrillar hydrogels, ubiquitous use in 3D biomaterials development, and highly conserved nature between species. Nevertheless, it should be noted that while there are differences in the structural and mechanical properties of collagens derived from various mammalian sources, these differences can stem from the specific isolation conditions and are seemingly equally influenced by gelation conditions (i.e., pH, temperature, and local geometry) than by species of origin.[115,116] This rat tail collagen I was diluted to a final concentration of 2.5 or 6 mg/mL in high-glucose DMEM cell culture medium (Gibco #12800082) and neutralized with 1N NaOH. PAAm bead stocks of varying stiffness were briefly spun down in a mini centrifuge, and the 1× PBS supernatant was aspirated before gently resuspending the beads in one of the prepared collagen solutions at a 6:1 ratio, respectively. Collagen solutions with and without beads were pipetted into PDMS microwells, such that the wells were slightly overfilled, and PDMS lids were oriented on top of the filled wells to avoid air bubbles. Hydrogels were polymerized via the cold-cast protocol as previously described.[53] In short, gels were allowed to incubate for 15 min at 4°C, room temperature, and 37°C and were flipped every 5 min during the polymerization process to ensure bead packing consistency throughout the gel. After a total of 45 min, the hydrogels were submerged in the high-glucose DMEM, the PDMS lids were removed, and the gels were stored at 37°C for 36 h. The hydrogels were finally fixed in 4% PFA for 25 min, then thoroughly washed and stored in 1× PBS at 4°C.

## BCA assay for collagen quantification

The collagen concentrations of pre-gel solutions were quantified using a micro-BCA protein assay (Thermo Scientific #23235). Experiments were conducted according to manufacturer specifications, with the following exceptions. Rat tail collagen type I solutions were serially diluted in milliQ water to eight final concentrations of 80, 40, 20, 10, 5, 2.5, 1, and 0.5 μg/mL and were used to establish experimental standard curves. Beadless collagen solutions (2.5 or 6 mg/mL) were prepared as previously described, and 1:6 collagen-to-bead mixtures were prepared from these stocks. These beadless and bead-laden collagen solutions were diluted in milliQ water to a target total collagen concentration of 40 μg/mL, excluding the bead volume fraction from the calculations. PAAm beads were allowed to settle out of the solutions during the colorimetric reaction, such that only the reacted collagen in the supernatant was analyzed. All absorbance measurements were acquired within 10 min of each other using a Beckman Coulter DU730 Life Science ultraviolet-visible (UV-vis) Spectrophotometer.

## Rheology

Rheological characterization was performed on a Discovery HR-3 rheometer (TA Instruments) with temperature calibration. An 8 mm parallel plate geometry and 500 μm gap distance were used for all tests. To avoid gel slippage, PEI and glutaraldehyde-treated glass coverslips were attached to both the top and bottom geometries. Gel solutions were loaded onto the rheometer in between the coverslips and allowed to gel *in situ* following the cold-casting protocol (15 min at 4°C, 15 min at 21°C, 30 min at 37°C).[53] To prevent dehydration, mineral oil (Sigma) was deposited around the sample. After 1 h of gelation, the final storage modulus was measured at 0.5% strain and 1 Hz for 60 s. Final storage moduli were calculated by averaging these measurements. Stress relaxation tests were performed at 15% strain for 300 s at 37°C with a strain rise time of 0.1 s (thus, the initial 0.1 s of measurements were discarded). To eliminate noise and to determine initial stress values, stress relaxation tests were smoothed with a Savitzky-Golay filter in SciPy with a window size of 25 and polynomial degree of 5.[57,117] To calculate the relaxation half-time ($\tau_{1/2}$), the smoothed data were fit to a 3-element Maxwell-Weichert model[57,118] (Figure S3A) using SciPy curve_fit, which can be described as:

$$\sigma = \sum_n \sigma_n e^{-t/\tau_n}.$$

## Cell culture

MDA-MB-231 (ATCC) and EO771-YFP (LanYFP-expressing, CH3-Biosystems, provided by the Schaffer-Nishimura lab at Cornell University) cells were cultured in 75 $cm^2$ flasks using high-glucose DMEM cell culture medium (Gibco #12800082) supplemented with 10% fetal bovine serum (FBS, Atlanta

Please cite this article in press as: Knode et al., Adipose-mimetic granular hydrogels uncover biophysical cues driving breast cancer invasion, Cell Biomaterials (2026), https://doi.org/10.1016/j.celbio.2026.100411



Biologicals #S11150) and 1% penicillin/streptomycin (Gibco #15070063). MCF10A cells (ATCC) were similarly cultured using high-glucose DMEM/F12 culture medium supplemented with 5% horse serum (Thermo Scientific #16050122), 10 μg/mL insulin (Krackeler Scientific #45-91077C), 500 ng/mL hydrocortisone (Thermo Scientific Chemicals #A16292-03), 100 ng/mL cholera toxin (Krackeler Scientific #45-C8052), 20 ng/mL epidermal growth factor (EGF) (Invitrogen #PHG0313), and 1% penicillin/streptomycin. Cells were incubated at 37°C in an atmosphere of 5% $CO_2$ and maintained for experimental use until passage 20.

### Invasion and migration assays

Breast cancer cells were suspended in the appropriate high-glucose DMEM cell culture medium at a concentration of ~133,333 cells/mL. For endpoint experiments, polymerized hydrogels were submerged in 1.5 mL of this cell suspension and incubated at 37°C/5% $CO_2$ for 36 h. For live cell tracking, the cell suspension was first incubated with 100 ng/mL Hoechst stain (Thermo Scientific #H3570) for 45 min at 37°C, then centrifuged and resuspended in fresh media. Hydrogels cast in glass-bottomed culture dishes were submerged in 2 mL of this cell suspension and incubated at 37°C/5% $CO_2$ for 21 h during spinning disk confocal image acquisition. After incubation, all hydrogels were removed from cell suspension, fixed in 4% PFA solution for 25 min, then thoroughly washed and stored in 1× PBS at 4°C.

### Immunofluorescence

Fixed hydrogels were submerged in a permeabilization solution comprised of 0.1% Triton X-100 (Thermo Scientific #AAA16046AP) and 1% BSA (Fisher Scientific #BP1600-100) in 1× PBS for 15 min at room temperature. Permeabilization solution was aspirated, and a 132 nM solution of Alexa Fluor 568-conjugated phalloidin (Thermo Scientific #A12380) in 1× PBS + 1% BSA was pipetted on top of the exposed hydrogel surface in a small-volume bleb. The staining solution was allowed to incubate for 45 min at room temperature. This process was repeated a second time to ensure proper diffusion of the staining solution throughout the gel. The hydrogels were lastly submerged in a 715 nM solution of DAPI (Thermo Scientific #D1306) in 1× PBS + 1% BSA for 30 min at room temperature before being rinsed and stored in 1× PBS at 4°C.

### Confocal microscopy

For 36-h endpoint experiments, PDMS ring-encapsulated hydrogels were removed from the 12-well plate, inverted, and mounted in 1× PBS on a 24 × 60 mm no. 1 glass coverslip (VWR #48404-455). Representative image stacks were acquired on a Zeiss LSM880 confocal multiphoton inverted microscope using a C-Achroplan 32×/0.85 W Corr M27 objective. z stack images of the top 150 μm of each gel were acquired with step sizes of 4 or 5 μm, each slice measuring 512 pixels × 512 pixels. The Zeiss Zen Smart Setup function was used to configure fluorescence channels for DAPI, Alexa Fluor 488, and Alexa Fluor 568 visualization. Reflectance imaging was used to evaluate collagen fiber structures, for which a customized reflectance channel was added to the Smart Setup configuration.

For live cell tracking experiments, time-lapse image stacks were acquired on an Olympus IX83 inverted spinning disk confocal microscope using a 10×/0.4 air objective. Two fluorescence channels were configured to visualize DAPI and Alexa Fluor 488 signals. z stack images of the top 100 μm of the gels (5 μm step size) were acquired every 15 min over 21 h, and three representative fields of view were collected for the hydrogel imaged.

### Mammary tumor imaging window implantation

Four 6-month-old female C57BL/6 mice (The Jackson Laboratory) were anesthetized using isoflurane inhalation. LanYFP-expressing EO771 mammary carcinoma cells ($1 \times 10^4$ cells in 20 μL PBS) were orthotopically injected into the third mammary fat pad under aseptic conditions. Tumor growth was monitored by palpation. 2 weeks post injection, when palpable tumors were established, animals underwent surgical implantation of a mammary imaging window. Briefly, after hair removal and disinfection, a circular titanium frame (12 mm inner diameter; APJ Trading) was positioned over the tumor region and secured to the skin using interrupted sutures. A sterile glass coverslip (no. 1 thickness) was affixed over the frame to enable repeated optical access to the tumor microenvironment as described previously.[65]

### Intravital two-photon microscopy

Intravital imaging was performed using a multiphoton microscope equipped with a Chameleon Ti:sapphire laser (Coherent) tuned to 830 nm for excitation as published previously.[66] Fluorescence was collected in three detection channels of the microscope formed by three long-pass dichroics: LM01-488, FF560-Di02, and FF593-Di03. In addition, the channels had the following bandpass filters, respectively: FF01-417/60, FF01-517/65, and FF01-629/53. SHG signal was collected for collagen fibers, and fluorescence signal was collected for LanYFP tumor cells and Texas Red-dextran-labeled blood plasma (70 kDa; Thermo Fisher Scientific, 30 μL of 2.5% in saline injected intravenously). Imaging was conducted with a 20× water-immersion objective at 37°C. Two to three representative regions of interest (ROIs) measuring at least 216 μm × 216 μm × 100 μm (512 pixels × 512 pixels × 100 voxels) were acquired for each mouse across several time points. Care was taken to maintain anesthesia throughout imaging in accordance with Cornell University IACUC protocol (2015-0029).

### Image analysis

All acquired images were processed and analyzed using the open-source image analysis software ImageJ/Fiji,[119] unless otherwise noted. Sample counts for each analysis are included in the respective subsection and comprise at least three biological replicates unless stated differently.

#### *Adipocyte/PAAm bead characterization*

To evaluate the distribution of adipocyte diameters in murine adipose tissue, histological sections stained with Masson's trichrome were evaluated. The areas of individual adipocyte cross-sections were evaluated, and undeformed adipocyte diameters $d$ were calculated using $A = \pi\left(\frac{d}{2}\right)^2$, where $A$ is the

adipocyte cross-sectional area. 1,626 individual adipocyte cross-sections were analyzed, collected from 5 mice. Similarly, to analyze the diameter distributions of PAAm bead batches, bright-field images of PAAm beads were acquired and manually traced in ImageJ/Fiji. Since PAAm beads maintain high sphericity after polymerization, the diameters of individual beads were directly traced rather than using the circumference to infer an approximate diameter.

Confocal image stacks were utilized to analyze the local packing fraction of PAAm beads within each collagen hydrogel condition via the tracking of bead centers and diameters. One z stack was acquired for each condition, and each stack depicted ~6 layers of bead packings. First, a circular Hough transform was used in MATLAB to identify the circular cross-sections along with their centers and radii in each image slice. We denote the x-y plane to be parallel to the image slice and the z-direction parallel to the confocal microscopy scanning direction. Second, we identify whether circular cross-sections from different z-slices belong to the same bead. Any circles whose centers are no more than 0.1 of the bead diameter apart along the x-y plane and no more than the bead diameter apart along the z-direction are deemed to belong to the same bead. Third, using the x, y, and z positions of all circular cross-sections deemed to be from the same bead, we obtain the center and radius of that bead through least-squares fitting to the equation for a sphere. After determining the centers and radii of the beads, we further calculate the local packing fraction for each tracked bead. To do this, we first apply a Voronoi tessellation to the bead packing using Voro++.[64] We then calculate the local packing fraction, defined as the bead volume divided by the volume of its associated Voronoi polyhedron. Since a Voronoi polyhedron contains both the hydrogel spheres and void space, and all Voronoi polyhedral together tessellate the entire space, the local packing fraction accurately describes the void space.

### Collagen fiber network analyses

Granular hydrogel collagen fiber characteristics were analyzed using multiple computational platforms, and 150-μm image stacks collected from 5 ROIs in each condition were first corrected to eliminate noise. Confocal reflectance microscopy visualization of these collagen hydrogel networks yielded raw micrographs with high background signal and a central artifact that interfered with downstream analyses. To minimize the contaminating noise, all raw reflectance images were subjected to the ImageJ/Fiji "subtract background" function at a sigma value of 5 pixels. To eliminate the central reflectance artifact, the ImageJ/Fiji "image calculator" was used to identify the artifact via overlap of multiple image slices ("AND" function) and then subtract the isolated artifact from each raw image slice ("SUBTRACT" function), after which image stacks were automatically thresholded using the "triangle" filter.

The collagen fiber networks in living murine adipose tissue were similarly analyzed using SHG images collected from intravital two-photon microscopy of mammary tumors and adjacent adipose tissue. SHG image stacks (150 μm × 150 μm × 40 μm [xyz] with a step size of 1 μm) were collected from four mice (multiple ROIs of the same tumor per mouse). Three replicate image stacks per condition were used for analysis of different tissue structures: highly fibrotic or less fibrotic, with or without packed adipocytes (adipocyte identification details below). To address the high background signal, which is characteristic of intravital imaging, and better illuminate the collagen structures to be characterized, the ImageJ/Fiji subtract background function was applied at a sigma value of 10 pixels (4.22 μm). Image stacks were then split, and 5 μm maximum projections were restacked as "slices" to mirror *in vitro* data dimensions. After reslicing, contrast was enhanced to a saturation level of 0.1% and normalized across the stack, then background signal was again subtracted to illuminate fibrillar structures. Finally, for downstream analyses, duplicate gamma-manipulated (0.5) image stacks were automatically thresholded using the "moments" filter across the stack histogram, and the resulting mask was applied to the corrected collagen ROI. To quantify the differences in fibrosis between representative fields of view, the ImageJ/Fiji "histogram" function was used to calculate the number of positive (above threshold) and negative (background) pixels for each binarized slice. The average ratio of these values was computed for each representative stack and compared between conditions such that a larger positive pixel fraction was indicative of increased fibrosis.

The alignment of collagen fibers both *in vitro* and *in vivo* was evaluated using the ImageJ/Fiji plugin OrientationJ "analysis" function, as has been previously reported.[63] In short, fiber "coherency" defines the relative orientation of locally defined image features by employing a gradient structure tensor that accounts for relevant directional information, whereby a coherency score of 1 is suggestive of perfect anisotropy at the defined scale and a score of 0 indicates local fiber isotropy. For this specific protocol, a local window size of 6 pixels, approximating the size of a focal adhesion complex,[120] was used to survey confocal reflectance microscopy images of collagen fibers via the cubic spline method. To account for differences in pixel resolution, the same protocol was applied to *in vivo* SHG images with a local window size of 7 pixels. Image output parameters were adjusted such that the hue of the collagen network corresponded to the local fiber coherency score. The RGB (red, green, blue) images resulting from this color survey were converted to HSB (hue, saturation, brightness) stacks, from which the hue channel was isolated, and 8-bit histogram values (0–255) were collected. 8-bit values were converted to a 0–1 scoring scale corresponding to fiber coherency scores, and score distributions were evaluated for outliers using the GraphPad Prism ROUT (robust regression and outlier removal) method. The maximum desired false discovery rate (FDR), denoted by the variable Q, was set equal to 1%. Identified outliers were removed, and cleaned datasets were analyzed to draw conclusions about local collagen fiber alignment.

Granular hydrogel collagen fiber interconnectivity was observed and characterized by thresholding the aforementioned hue channel of each color-surveyed image at intervals corresponding to coherency scores from 0 to 1. The "3D object counter" function was then used to identify fiber clusters greater than 250 $\mu m^3$ in volume so that any remaining reflectance artifacts and/or single collagen fibers were removed from the binarized output image. Each binary 3D object identified a distinct cluster of interconnected fibers, and the volumes of these objects were collected at each coherency score threshold. The overall matrix connectivity score at each threshold level was defined as follows:

Please cite this article in press as: Knode et al., Adipose-mimetic granular hydrogels uncover biophysical cues driving breast cancer invasion, Cell Biomaterials (2026), https://doi.org/10.1016/j.celbio.2026.100411



$$connectivity = \frac{V_{large}}{V_{total}},$$

where $V_{large}$ is the total volume of all identified large objects (large, interconnected fibers) and $V_{total}$ is the total volume of all identified objects (both small, single fibers and large, interconnected fibers) after coherency score thresholding. The connectivity score measures the volume fraction of large, interconnected collagen fibers among all collagen fibers. The connectivity score ranges between 0 and 1 (or 0 and 100, depending on whether we want to use percentages), with 0 indicating no presence of large fibers and 1 indicating all identified collagen fibers are interconnected. Connectivity scores were calculated for each coherency score threshold level and compared between mechanically distinct hydrogel conditions.

To further analyze the local alignment of the collagen fibers,[121] a subset of confocal images (one z stack, 31 slices per condition) of collagen was divided into small, overlapping 20.75 μm by 20.75 μm windows (or 40 pixels × 40 pixels, with each two adjacent windows overlapping by 50%). Then, each window was transformed into a window with the same size F in the Fourier space using a 2D fast Fourier transform (FFT). The central image moments of the FFT were calculated as follows:

$$M_{00} = \sum_{i=1}^{40}\sum_{j=1}^{40} F_{ij},$$

$$M_{10} = \sum_{i=1}^{40}\sum_{j=1}^{40} iF_{ij},$$

$$M_{01} = \sum_{i=1}^{40}\sum_{j=1}^{40} jF_{ij},$$

$$M_{11} = \sum_{i=1}^{40}\sum_{j=1}^{40} ijF_{ij},$$

$$M_{20} = \sum_{i=1}^{40}\sum_{j=1}^{40} i^2F_{ij},$$

$$M_{02} = \sum_{i=1}^{40}\sum_{j=1}^{40} j^2F_{ij},$$

where i and j are indices of a pixel along the horizontal and vertical directions, respectively, and $F_{ij}$ is the value of the Fourier-transformed window at pixel (i, j). The central moments were then used to construct the 2 by 2 symmetric covariance matrix of the window image:

$$C = \begin{pmatrix} \frac{M_{20}}{M_{00}} - \left(\frac{M_{10}}{M_{00}}\right)^2 & \frac{M_{11}}{M_{00}} - \frac{M_{10}M_{01}}{(M_{00})^2} \\ \frac{M_{11}}{M_{00}} - \frac{M_{10}M_{01}}{(M_{00})^2} & \frac{M_{02}}{M_{00}} - \left(\frac{M_{01}}{M_{00}}\right)^2 \end{pmatrix}.$$

The direction of the eigenvector corresponding to the larger eigenvalue of C reveals the direction of collagen fibers in that window, θ, and the eigenvalues ($\lambda_1$ and $\lambda_2$) of C are used to calculate the eccentricity of collagen fiber alignment, $e=|\lambda_1 - \lambda_2|/(\lambda_1 + \lambda_2)$. The eccentricity ranges between 0 and 1, with 0 corresponding to random collagen orientations and 1 corresponding to perfect collagen fiber alignment. Windows with low enough image intensity (10% of the highest image intensity) were ignored for this analysis.

Lastly, the same subset of confocal image slices (one z stack, 31 slices per condition) was used to evaluate the structural characteristics of individual collagen fibers using the independent MATLAB application CurveAlign.[122] To measure the approximate length, width, and straightness of individual collagen fibers, corrected reflectance images of collagen networks were opened in the CT-Fire function of the CurveAlign application. CT-Fire parameters were configured as follows: "thresh_im2" = 15, "s_xlinkbox" = 5, minimum fiber length = 4 pixels, fiber line width = 0.5, maximum fiber width = 50 pixels, and the percentile of remaining curvelet coefficients was set to 0.2. Output fiber length, width, and straightness distributions were averaged and compared between the mechanically distinct hydrogel conditions.

### Cancer cell invasion analyses

MDA-MB-231 cell invasion through control and bead-laden collagen hydrogels was investigated by tracking individual cell nuclei in the z-direction after 36 h of invasion. For each mechanical condition, 4 confocal image stacks were analyzed, and DAPI-labeled nuclei were identified using the TrackMate plugin configured with the StarDist tracker for segmentation.[123,124] All TrackMate parameters remained set to the default values with the exception of the following adjustments: auto quality and contrast filters were applied, a simple LAP (linear assignment problem) tracker was used to track individual nuclei, the linking max distance was set to 5 pixels, the gap-closing max distance to 5 pixels, and the gap-closing max frame gap to 1 frame interval. Display tracks were excluded, and a label image including spots corresponding to tracks was exported for further analysis. The Fiji 3D Objects analysis tool was then used to evaluate the localization of individual nuclei throughout the acquired z stack, and the centroid measurement of any object greater than 100 voxels in volume was recorded. The invasion depth of cells was calculated after a 36-h incubation period as follows:

$$invasion\ depth = (centroid\ slice\ value - 1) \times (step\ size\ in\ \mu m).$$

Additionally, the diffusion constant was calculated for the same populations of cells. If we assume that the cancer cells move diffusively at long time scales (e.g., within hours), for each of the six mechanical conditions, the probability distribution of the invasion depth $z$ follows a half-Gaussian distribution[59]:

$$P(z) = \sqrt{\frac{2}{\pi\sigma^2}}\exp\left(\frac{-z^2}{2\sigma^2}\right), z > 0,$$

where $\sigma = \sqrt{2Dt}$, $D$ is the diffusion constant of the cancer cells, and $t$ is the time elapsed since the beginning of the experiment. The cumulative distribution for a half-Gaussian process is

$$C(z) = erf\left(\frac{z}{\sigma\sqrt{2}}\right) = \frac{2}{\sqrt{\pi}}\int_0^{\frac{z}{\sigma\sqrt{2}}} e^{-s^2} ds.$$

The experimentally measured mean of the invasion depth $\bar{z}$ will converge to $\sigma\sqrt{\frac{2}{\pi}}$ as the number of experimental measurements increases. Thus, we can calculate $\sigma = \bar{z}\sqrt{\frac{\pi}{2}}$ and the resulting diffusion constant

$$D = \frac{\pi}{4t}\bar{z}^2$$

from the experimental measurements of the invasion. The cumulative distribution of the experimentally measured invasion depths and from an ideal half-Gaussian process with the best-fit values of $\sigma$ (and corresponding $R^2$ values) are shown in Figures S5A and S5B.

Confocal micrographs of MDA-MB-231 cell nuclei squeezing between collagen-embedded PAAm beads were evaluated computationally to identify differences in nuclear deformation, and the shapes of the deformed nuclei were compared with those of unconfined nuclei. First, 15 confined nuclei were isolated from the segmented image stacks of each of the four bead-laden hydrogel conditions, and nuclei selected for this analysis were in contact with two or more PAAm beads in the same x-y plane. Similarly, 15 nuclei uncontacted by PAAm beads during image acquisition were isolated from the same segmented image stacks. The nuclei of cells invading through beadless collagen hydrogels were also isolated for comparison. Lastly, the dimensionality of each isolated nucleus was reduced via maximum intensity projection, and 2D nuclear roundness was calculated by applying the Fiji "measure" function to each replicate image.

A similar method was employed to characterize the deformation of PAAm beads in contact with migratory cancer cells. Confocal image stacks of PAAm bead hydrogels, including and excluding cancer cells, were surveyed, and at least 60 beads were manually segmented for each condition. Undeformed bead metrics were collected from image stacks of hydrogels not seeded with MDA-MB-231 cells, while deformed beads were defined as those in contact with and contributing to the confinement of migratory cell nuclei. Individual bead roundness was evaluated for all conditions by isolating the x-y plane at which the bead of interest was most visually deformed, then characterizing this segmented slice using the Fiji measure function.

The same technique was applied to characterize the deformation of adipocytes *in vivo*. Briefly, intravital SHG (collagen) and fluorescent (separate EO771 and blood plasma) images collected from three tumor-bearing mice were overlaid, and adipocyte boundaries were manually traced from each representative stack. The fluorescent dextran intended for vasculature labeling also diffused into surrounding tissue structures, presumably due to leaky tumor vasculature, and provided good contrast for adipocyte tracing. Adipocytes were identified as any relatively spherical volume of 3D void spaces greater than 20 μm in diameter. Adipocyte cross-sections were manually segmented slice by slice, and regions of high and low cancer cell invasion were identified. Overlaying this masked stack with the corresponding EO771 image stack, adipocyte cross-sections that were in contact with confined cancer cells were isolated for analysis. Adipocyte cross-sections that were not in contact with confined cancer cells served as undeformed controls. Five representative cell masks for each sample type were collected from each image stack and were evaluated using the Fiji measure function to determine roundness and circularity values.

To characterize live cell invasion data acquired via spinning disk confocal microscopy, it was first necessary to track cancer cell nuclei localization over the time course. We identified cell nuclei centers at each time step. To do so, at a given time step, we binarized images taken from spinning disk microscopy at all z stacks and then used the "regionprops3" function in MATLAB to identify voxels that belonged to each cell nucleus. We then calculated the center of mass for each nucleus as the center for that nucleus. After identifying all cell nuclei centers from all time steps, we implemented the method described by Crocker and Grier[125] to track the cells. We calculated the speed of a cell at a given time step as the displacement of that cell from the previous time step to the current time step divided by the time interval.

Furthermore, the relationship between the bead packing fraction and cell acceleration was evaluated by calculating the distance between a migratory cell's nuclear centroid and the surface of nearby beads tracked from the spinning disk image stacks. It was first necessary to determine the precise packing of PAAm beads throughout the acquired region of interest. z stacks were surveyed manually, whereby the largest x-y spherical cross-section of each bead was segmented and duplicated into a temporary stack, maintaining the dimensionality of the original images. These segmented stacks were then uploaded to the 3D modeling software Dragonfly (license #BNR90-30900-G1HJK-M8P9Q-911AH-KPYED-GNU89KDUV) and the "create a sphere" shape tool was used to reconstruct the volume of each bead throughout the stack. This was achieved by aligning the radius and center of a sphere with that of a segmented bead cross-section, then replacing image stack data contained within the spherical region with saturated pixels using the "image operations" overwrite function. Once all bead volumes were reconstructed, the resulting stack was exported and then merged with the original segmented nuclear channel in Fiji, and the localization of migratory nuclei between PAAm beads was quantified for every time point. Using the centers and radii of tracked beads, we calculated the distance between the centroid of a nucleus of interest and its nearest neighboring bead. Finally, the cell accelerations were determined from the migratory speed datasets and then correlated with the degree of local confinement (bead proximity) calculated for each time point.

### DEM modeling of breast cancer and adipocytes

Adipocytes are modeled as deformable particles and breast cancer cells as adhesive soft disks in 2D. The total energy of the system is given by

$$U = U_a + U_{aa} + U_{cc} + U_{ac} + U_w,$$

where $U_a$ is the total shape energy of the adipocytes, $U_{aa}$ is the total interaction energy between adipocytes, $U_{cc}$ is the total interaction energy between cancer cells, $U_{ac}$ is the total

Please cite this article in press as: Knode et al., Adipose-mimetic granular hydrogels uncover biophysical cues driving breast cancer invasion, Cell Biomaterials (2026), https://doi.org/10.1016/j.celbio.2026.100411



CellPress

interaction energy between adipocytes and cancer cells, and $U_w$ is the total interaction energy between both adipocytes and cancer cells and the confining walls. Each adipocyte is modeled as a deformable polygon with $N_v$ vertices, and $U_a$ is given by

$$U_a = \sum_{\alpha}^{N_\alpha} \frac{1}{2}\varepsilon_a \left(1 - \frac{a_\alpha}{a_{\alpha,0}}\right)^2 + \sum_{\alpha}^{N_\alpha} \sum_{i}^{N_v} \frac{1}{2}\varepsilon_l \left(1 - \frac{l_{\alpha,i}}{l_{\alpha,0}}\right)^2 + \sum_{\alpha}^{N_\alpha} \sum_{i}^{N_v} \frac{1}{2}\varepsilon_b \left(\theta_{\alpha,i} - \theta_{\alpha,0}\right)^2,$$

where $N_\alpha$ is the total number of adipocytes; $a_\alpha$ is the area of adipocyte $\alpha$ with a preferred area $a_{\alpha,0}$; $l_{\alpha,i}$ is the length between vertices i and (i+1) with a preferred length $l_{\alpha,0}$; and $\theta_{\alpha,i}$ is the angle formed by vertices (i-1), i, and (i+1) with a preferred angle $\theta_{\alpha,0}$. $\varepsilon_a$, $\varepsilon_l$, and $\varepsilon_b$ are the energy scales that control deviations of adipocyte area, perimeter, and local curvature from their rest values, respectively (see Figure 5A).

To prevent adipocytes from interpenetrating, we include an energy penalty when two adipocytes overlap:

$$U_{aa} = \sum_{\alpha}^{N_\alpha} \sum_{\beta>\alpha}^{N_\beta} \sum_{i}^{N_v} \sum_{j}^{N_v} \frac{1}{2}\varepsilon_{aa} \left(1 - \frac{r_{\alpha i,\beta j}}{\sigma_{\alpha i,\beta j}}\right)^2 \Theta\left(1 - \frac{r_{\alpha i,\beta j}}{\sigma_{\alpha i,\beta j}}\right),$$

where $r_{\alpha i,\beta j}$ is the distance between vertex i on adipocyte $\alpha$ and vertex j on adipocyte $\beta$, $\sigma_{\alpha i,\beta j}$ is the sum of the radii of vertex i on adipocyte $\alpha$ and vertex j on adipocyte $\beta$, $\varepsilon_{aa}$ is the repulsive energy scale, and $\Theta(\cdot)$ is the Heaviside step function (see Figure 5A). $N_c$ cancer cells interact pairwise via the following energy:

$$U_{cc} = \begin{cases} \sum_{n}^{N_c} \sum_{m>n}^{N_c} \frac{1}{2}\varepsilon_{cc} \left(\left(1 - \frac{r_{nm}}{\sigma_{nm}}\right)^2 - \frac{1}{2}\zeta a_c^2\right), r_{nm} \le \sigma_{nm} \\ \sum_{p}^{N_c} \sum_{q}^{N_c} \frac{1}{2}\zeta\varepsilon_{cc} \left(\left(1 - \frac{r_{nm}}{\sigma_{nm}}\right)^2 - \frac{1}{2}a_c^2\right), \sigma_{nm} < r_{pq} \le (1+0.5a_c)\sigma_{nm} \\ \sum_{p}^{N_c} \sum_{q}^{N_c} -\frac{1}{2}\zeta\varepsilon_{cc} \left(1 + a_c - \frac{r_{nm}}{\sigma_{nm}}\right)^2, (1+0.5a_c)\sigma_{nm} < r_{pq} \le (1+a_c)\sigma_{nm} \\ 0, otherwise, \end{cases}$$

where $r_{nm}$ is the distance between cancer cells n and m, $\sigma_{nm}$ is the sum of the radii of cancer cells n and m, $a_c$ sets the attraction range, $\varepsilon_{cc}$ is the energy scale, and $\zeta$ sets the attraction strength. The resultant force is shown in Figure 5A. Adipocytes and cancer cells interact via purely repulsive forces given by the gradient of the following potential energy:

$$U_{ac} = \sum_{\alpha}^{N_\alpha} \sum_{i}^{N_v} \sum_{n}^{N_c} \frac{1}{2}\varepsilon_{ac} \left(1 - \frac{r_{\alpha i,n}}{\sigma_{\alpha i,n}}\right)^2 \Theta\left(1 - \frac{r_{\alpha i,n}}{\sigma_{\alpha i,n}}\right),$$

where $r_{\alpha i,n}$ is the distance between vertex i on adipocyte $\alpha$ and cancer cell n, and $\sigma_{\alpha i,n}$ is the sum of radii of vertex i on adipocyte $\alpha$ and cancer cell n. Packings of adipocytes and cancer cells are confined within a rectangular box with area $L_xL_y$ and periodic boundary conditions in the y-direction and confined by two walls in the x-direction (see Figure 5A). One wall is fixed at $x = 0$, and the other is positioned at $x = L_x$. Both adipocytes and cancer cells interact with the walls via purely repulsive forces that are generated via the gradient of the following potential energy:

$$U_w = \sum_{\alpha}^{N_a} \sum_{i}^{N_v} \frac{1}{2}\varepsilon_w \left(1 - \frac{x_{\alpha i}}{0.5\sigma_{\alpha i}}\right)^2 \Theta\left(1 - \frac{x_{\alpha i}}{0.5\sigma_i}\right) + \sum_{\alpha}^{N_a} \sum_{i}^{N_v} \frac{1}{2}\varepsilon_w \left(1 - \frac{L_x - x_{\alpha i}}{0.5\sigma_{\alpha i}}\right)^2 \Theta\left(1 - \frac{L_x - x_{\alpha i}}{0.5\sigma_i}\right) + \sum_{n}^{N_c} \frac{1}{2}\varepsilon_w \left(1 - \frac{x_n}{0.5\sigma_n}\right)^2 \Theta\left(1 - \frac{x_n}{0.5\sigma_n}\right) + \sum_{n}^{N_c} \frac{1}{2}\varepsilon_w \left(1 - \frac{L_x - x_n}{0.5\sigma_n}\right)^2 \Theta\left(1 - \frac{L_x - x_n}{0.5\sigma_n}\right),$$

where $x_{\alpha i}$ and $x_n$ are the x-positions of vertex i on adipocyte $\alpha$ and cancer cell n, respectively; $\sigma_{\alpha i}$ and $\sigma_n$ are the diameters of vertex i on adipocyte $\alpha$ and cancer cell n, respectively; and $\varepsilon_w$ is the energy scale of the interactions with the wall. The pressure $P$ in the system is given by the sum of all forces exerted on the wall at $L_x$, divided by $L_y$.

We study systems with $N_\alpha = 32$ adipocytes with half possessing $N_v = 20$ vertices and the other half possessing $N_v = 28$ vertices, and $N_c = 800$ cancer cells. For each adipocyte, we set the shape parameter $\mathcal{A} = (N_v l_{\alpha,0})^2/(4\pi a_{\alpha,0}) = 1$ and $\theta_{\alpha,0} = 2\pi/N_v$, such that a stress-free adipocyte possesses the shape of a regular polygon with $N_v$ sides. We set $a_{\alpha,0} = 5,000\ \mu m^2$ $(10,000\ \mu m^2)$ for the small (large) adipocytes with $N_v = 20$ $(28)$ so that the average adipocyte diameter is $\langle D_a \rangle = 100\ \mu m$. We draw the diameters of cancer cells from a uniform distribution with mean $\langle \sigma_n \rangle = 0.1\langle D_a \rangle = 10\ \mu m$ and SD $\delta_\sigma/\langle \sigma_n \rangle = 0.1$. We set $\varepsilon_a = 0.05J$ so that it is comparable to the bulk modulus of a lipid droplet ($\varepsilon_a/a_{\alpha,0} \sim 10MPa$).[126] Furthermore, we set $\varepsilon_l/\varepsilon_a = 0.1$, $\varepsilon_{aa}/\varepsilon_a = 0.1$, $\varepsilon_{cc}/\varepsilon_a = 0.05$, $\varepsilon_{ac}/\varepsilon_a = 0.1$, $\varepsilon_w/\varepsilon_a = 0.1$, $\zeta = 0.01$, and $a_c = 0.1$. We vary $\varepsilon_b/\varepsilon_a$ from $10^{-4}$ to $10^{-2}$ to study the effect of adipocyte stiffness on breast cancer invasion.

### Compressive stiffness of an adipocyte

To characterize the compressive stiffness of an adipocyte, we place the adipocyte between two rigid walls. The adipocyte interacts with the walls via $U_w$. We decrease the distance between two walls by a small amount and perform energy minimization for

Please cite this article in press as: Knode et al., Adipose-mimetic granular hydrogels uncover biophysical cues driving breast cancer invasion, Cell Biomaterials (2026), https://doi.org/10.1016/j.celbio.2026.100411



the adipocyte. We then measure the force exerted on the walls. We repeat this process iteratively and determine the compressive stiffness as the slope of the wall force versus the adipocyte compressive strain.

### Initial adipocyte-cancer cell packing

For the simulations of cancer cell invasion into adipose tissue, we first generate a static packing of adipocytes and breast cancer cells with an abrupt interface at a target pressure $P_t$. To prevent adipocytes from mixing with cancer cells in the static packing, we initially generate the adipocyte packing and the cancer cell packing separately and then put them together. To generate an adipocyte packing, we start from a dilute packing with packing fraction $\phi = 0.01$ in a square box (with the same lengths $L_{x,a}$ and $L_{y,a}$ along the x- and y-directions) with two straight walls to confine the packing in the $x$-direction and periodic boundary conditions in the $y$-direction in 2D. We then compress the packing by reducing $L_{x,a}$ and $L_{y,a}$ by the same amount with a change in packing fraction $\Delta\phi = 0.001$, followed by energy minimization. If $P$ is smaller than $P_t$, we compress the packing again. Otherwise, we return to the packing before the compression and compress the system by half of the original $\Delta\phi$. We repeat this process until we reach $P_t$ to within $P_t \pm 0.01P_t$. We apply the same procedure to generate a packing of breast cancer cells in a box with length in the y-direction $L_{y,c} = L_{y,a}$, and we only change the box length along the x-direction $L_{x,c}$ to compress or decompress to achieve $P_t$. We then join the adipocyte and breast cancer cell packings and repeat the compression and decompression procedure by changing only the box length along the x-direction until $P$ of the entire packing reaches $P_t$ to within $P_t \pm 0.01P_t$.

### Breast cancer invasion

After generating a static packing of adipocytes and cancer cells, we study a system of cancer cells driven by thermal fluctuations to migrate through the adipocyte packing. To do so, we assign velocities to the cancer cells drawn from a Gaussian distribution with zero mean in both the x- and y-directions and a variance determined by the temperature T. We then carry out constant temperature and pressure molecular dynamics simulations. The equations of motion for the cancer cells, adipocytes, and the mobile wall are given by:

$$m_{\alpha i}\frac{d^2\vec{r}_{\alpha,i}}{dt^2} = \frac{\partial U}{\partial \vec{r}_{\alpha i}} - \gamma\frac{d\vec{r}_{\alpha i}}{dt},$$

$$m_n\frac{d^2\vec{r}_n}{dt^2} = \frac{\partial U}{\partial \vec{r}_n} - \gamma\frac{d\vec{r}_n}{dt} + \sqrt{2T\gamma m_n}\vec{\eta}(t),$$

$$m_w\frac{d^2L_x}{dt^2} = -P_tL_y - \frac{\partial U_w}{\partial L_x} - \gamma\frac{dL_x}{dt},$$

where $m_{\alpha i}$, $m_n$, and $m_w$ are the masses of vertex i on adipocyte $\alpha$, cancer cell n, and mobile walls, respectively; $\vec{r}_{\alpha,i}$, $\vec{r}_n$, and $L_x$ are the positions of vertex i on adipocyte $\alpha$, cancer cell n, and mobile walls, respectively; $\gamma$ is the damping coefficient; and $\vec{\eta}(t)$ is a 2D Gaussian noise strength that has zero mean and unit SD in both the x- and y-directions and zero covariance. We use the cancer cell diameter (10 μm) and mean speed of motile cancer cells in the bead-collagen mixture (under 20 μm/h) to set the length and time scales of the simulations. We note that the mean cancer cell migration speed is comparable to the ones observed in isolation on a substrate.[67] In addition, since we are mainly focusing on the effects of adipocyte stiffness, we expect the results to be relatively insensitive to the short-time dynamics of the cancer cell motility model.

### Characterization of the degree of invasion

We quantify the degree of invasion by calculating the interface length between adipocytes and breast cancer cells. Specifically, we apply the Laguerre-Voronoi tessellation based on the positions of cancer cells and vertices of the adipocytes. After the Laguerre-Voronoi tessellation, a Voronoi polygon is associated with each breast cancer cell and adipocyte vertex. We identify all edges shared between two polygons. We discard edges shared between vertices that belong to the same adipocyte. We define the invasion degree as

$$L_{inv} = \frac{L_{ac}}{L_{ac}+L_{aa}+L_{aw}},$$

where $L_{ac}$, $L_{aa}$, and $L_{aw}$ are the total lengths of edges shared between adipocytes and cancer cells, between different adipocytes, and between adipocytes and walls, respectively. We further rescale $L_{inv}$ by its minimum $L_{min}$ and maximum $L_{max}$ so that the scaled invasion length $0 < L'_{inv} < 1$:

$$L'_{inv} = \frac{L_{inv} - L_{min}}{L_{max} - L_{min}}.$$

## Statistical methods

Statistical significance was evaluated by unpaired two-tailed Student's $t$ test for the comparison of two conditions and by one-way analysis of variance (ANOVA) followed by Tukey's test for multiple comparisons. Unless otherwise noted, $p < 0.05$ for all analyses, and significance is depicted by compact letter display notation (i.e., groups with the same letter are not statistically different, while groups with distinct letters are statistically different from each other). Averaged data are reported as the mean plus or minus the SD unless specified.

## RESOURCE AVAILABILITY

### Lead contact

Requests for further information and resources should be directed to and will be fulfilled by the lead author, Claudia Fischbach (cf99@cornell.edu).

### Materials availability

This study did not generate any new, unique reagents.

### Data and code availability

All data reported in this paper will be shared by the lead contact upon reasonable request. This paper does not report original code. Any additional information required to reanalyze the data reported in this paper is available from the lead contact upon request.

## ACKNOWLEDGMENTS

We thank all members of the Fischbach Lab for valuable discussion and input during the preparation of this manuscript, Rebecca Williams for assistance with confocal microscopy, Ben Hopkins at WCM for help with generating *in vivo* tumors invading adipose tissue, the Cornell Center for Animal Resources and Education (CARE) for assistance with animal studies, the Cornell Animal Health Diagnostic Core for assistance with paraffin embedding and sectioning, the

Cornell Center for Materials Research shared instrumentation facility, and the Cornell Statistical Consulting Unit for assistance with statistical analysis. We acknowledge financial support from the NSF DGE2139899 (B.K.K), NCI F31CA278410 (G.F.B.), NCI R01CA259195 and R01CA276392 (C.F.), the Center on the Physics of Cancer Metabolism NCI 1U54CA210184 (C.F.), and the Cornell Engineering Learning Initiatives program. We also acknowledge support by a Rosalind Franklin fellowship from the Max Planck Centre for Physics in Medicine (C.F.); the European Union's Horizon 2020 research and innovation program grant no. 953121 (project FLAMIN-GO, S.G. and R.G.); and the Cornell Biotechnology Resource Center Imaging Facility funded by NYSTEM C029155, NIH S10OD018516, and NIH S10RR025502.

## AUTHOR CONTRIBUTIONS

B.K.K., G.F.B., C.S.O., and C.F. conceived and designed experiments. B.K.K. performed all experiments unless otherwise noted. B.K.K., G.F.B., and B.E.S. conducted initial system troubleshooting and protocol development. A. Bozec and G.F.B. collected murine adipose tissue for histological analysis and primary adipocyte isolation, established adipocyte and bead size distributions, and worked with A. Battistella to survey bead/adipocyte stiffness using AFM. S.G., J.G., and R.G. conceived, designed, and fabricated the adipocyte-mimetic PAAm beads. D.W. computationally evaluated granular hydrogel packing fraction, collagen fiber eccentricity, and adipocyte diameter accuracy, and aided B.K.K. in confocal image processing. B.K.K., D.W., and C.S.O. evaluated collagen fiber coherency data to define the network connectivity metric. Y.Z. calculated and analyzed breast cancer cell diffusion constants. C.-Y.E. and N.N. conceptualized and performed all intravital mammary fat pad imaging experiments, and B.K.K. processed the image data. I.K. designed, performed, and analyzed all rheology experiments. D.W. and C.S.O. employed DEM modeling to predict cancer cell invasion dependent on adipocyte stiffness. B.K.K. prepared all figures and schematics. B.K.K., G.F.B., D.W., and C.F. wrote the manuscript with input from all authors.

## DECLARATION OF INTERESTS

The authors declare no competing interests.

## SUPPLEMENTAL INFORMATION

Supplemental information can be found online at https://doi.org/10.1016/j.celbio.2026.100411.

Received: October 23, 2025
Revised: February 17, 2026
Accepted: February 20, 2026

## REFERENCES

1. Bray, F., Laversanne, M., Sung, H., Ferlay, J., Siegel, R.L., Soerjomataram, I., and Jemal, A. (2024). Global cancer statistics 2022: GLOBOCAN estimates of incidence and mortality worldwide for 36 cancers in 185 countries. CA Cancer J. Clin. *74*, 229–263. https://doi.org/10.3322/caac.21834.
2. Skibinski, A., and Kuperwasser, C. (2015). The origin of breast tumor heterogeneity. Oncogene *34*, 5309–5316. https://doi.org/10.1038/onc.2014.475.
3. van Zijl, F., Krupitza, G., and Mikulits, W. (2011). Initial steps of metastasis: Cell invasion and endothelial transmigration. Mutat. Res. *728*, 23–34. https://doi.org/10.1016/j.mrrev.2011.05.002.
4. Gupta, M., and Goyal, N. (2022). Applied Anatomy of Breast Cancer. In Breast Cancer: Comprehensive Management, S.C. Sharma, A. Mazumdar, and R. Kaushik, eds. (Springer Nature), pp. 23–35. https://doi.org/10.1007/978-981-16-4546-4_2.
5. Lintz, M., Muñoz, A., and Reinhart-King, C.A. (2017). The Mechanics of Single Cell and Collective Migration of Tumor Cells. J. Biomech. Eng. *139*, 210051–210059. https://doi.org/10.1115/1.4035121.
6. Haeger, A., Wolf, K., Zegers, M.M., and Friedl, P. (2015). Collective cell migration: guidance principles and hierarchies. Trends Cell Biol. *25*, 556–566. https://doi.org/10.1016/j.tcb.2015.06.003.
7. Lüönd, F., Tiede, S., and Christofori, G. (2021). Breast cancer as an example of tumour heterogeneity and tumour cell plasticity during malignant progression. Br. J. Cancer *125*, 164–175. https://doi.org/10.1038/s41416-021-01328-7.
8. Beeghly, G.F., Kopyeva, I., Deng, J., Pincus, M.I., Varshney, R.R., Giri, D.D., Falcone, D.J., Rudolph, M.C., Antonyak, M.A., Iyengar, N.M., and Fischbach, C. (2026). Large adipocytes increase vesicle-mediated lipid release and promote breast cancer malignancy. Cell Reports, 117061. https://doi.org/10.1016/j.celrep.2026.117061.
9. Ling, L., Mulligan, J.A., Ouyang, Y., Shimpi, A.A., Williams, R.M., Beeghly, G.F., Hopkins, B.D., Spector, J.A., Adie, S.G., and Fischbach, C. (2020). Obesity-associated Adipose Stromal Cells Promote Breast Cancer Invasion Through Direct Cell Contact and ECM Remodeling. Adv. Funct. Mater. *30*, 1910650. https://doi.org/10.1002/adfm.201910650.
10. Wu, Y., Li, X., Li, Q., Cheng, C., and Zheng, L. (2022). Adipose tissue-to-breast cancer crosstalk: Comprehensive insights. Biochim. Biophys. Acta Rev. Cancer *1877*, 188800. https://doi.org/10.1016/j.bbcan.2022.188800.
11. Corvera, S. (2021). Cellular Heterogeneity in Adipose Tissues. Annu. Rev. Physiol. *83*, 257–278. https://doi.org/10.1146/annurev-physiol-031620-095446.
12. Lynes, M.D., and Tseng, Y.H. (2018). Deciphering adipose tissue heterogeneity. Ann. N. Y. Acad. Sci. *1411*, 5–20. https://doi.org/10.1111/nyas.13398.
13. Kwok, K.H.M., Lam, K.S.L., and Xu, A. (2016). Heterogeneity of white adipose tissue: molecular basis and clinical implications. Exp. Mol. Med. *48*, e215. https://doi.org/10.1038/emm.2016.5.
14. Aboy-Pardal, M.C.M., Guadamillas, M.C., Guerrero, C.R., Català-Montoro, M., Toledano-Donado, M., Terrés-Domínguez, S., Pavón, D.M., Jiménez-Jiménez, V., Jimenez-Carretero, D., Zamai, M., et al. (2024). Plasma membrane remodeling determines adipocyte expansion and mechanical adaptability. Nat. Commun. *15*, 10102. https://doi.org/10.1038/s41467-024-54224-y.
15. Abuhattum, S., Kotzbeck, P., Schlüßler, R., Harger, A., Ariza de Schellenberger, A., Kim, K., Escolano, J.-C., Müller, T., Braun, J., Wabitsch, M., et al. (2022). Adipose cells and tissues soften with lipid accumulation while in diabetes adipose tissue stiffens. Sci. Rep. *12*, 10325. https://doi.org/10.1038/s41598-022-13324-9.
16. Hansson, B., Morén, B., Fryklund, C., Vliex, L., Wasserstrom, S., Albinsson, S., Berger, K., and Stenkula, K.G. (2019). Adipose cell size changes are associated with a drastic actin remodeling. Sci. Rep. *9*, 12941. https://doi.org/10.1038/s41598-019-49418-0.
17. Ghaben, A.L., and Scherer, P.E. (2019). Adipogenesis and metabolic health. Nat. Rev. Mol. Cell Biol. *20*, 242–258. https://doi.org/10.1038/s41580-018-0093-z.
18. Jääskeläinen, I., Petäistö, T., Mirzarazi Dahagi, E., Mahmoodi, M., Pihlajaniemi, T., Kaartinen, M.T., and Heljasvaara, R. (2023). Collagens Regulating Adipose Tissue Formation and Functions. Biomedicines *11*, 1412. https://doi.org/10.3390/biomedicines11051412.
19. Gliniak, C.M., Pedersen, L., and Scherer, P.E. (2023). Adipose tissue fibrosis: the unwanted houseguest invited by obesity. J. Endocrinol. *259*, e230180. https://doi.org/10.1530/JOE-23-0180.
20. Seo, B.R., Bhardwaj, P., Choi, S., Gonzalez, J., Andresen Eguiluz, R.C., Wang, K., Mohanan, S., Morris, P.G., Du, B., Zhou, X.K., et al. (2015). Obesity-dependent changes in interstitial ECM mechanics promote

breast tumorigenesis. Sci. Transl. Med. *7*, 301ra130. https://doi.org/10.1126/scitranslmed.3010467.

21. Ray, A., and Provenzano, P.P. (2021). Aligned Forces: Origins and Mechanisms of Cancer Dissemination Guided by Extracellular Matrix Architecture. Curr. Opin. Cell Biol. *72*, 63–71. https://doi.org/10.1016/j.ceb.2021.05.004.
22. Pathak, A., and Kumar, S. (2012). Independent regulation of tumor cell migration by matrix stiffness and confinement. Proc. Natl. Acad. Sci. USA *109*, 10334–10339. https://doi.org/10.1073/pnas.1118073109.
23. Fischer, R.S., Sun, X., Baird, M.A., Hourwitz, M.J., Seo, B.R., Pasapera, A.M., Mehta, S.B., Losert, W., Fischbach, C., Fourkas, J.T., et al. (2021). Contractility, focal adhesion orientation, and stress fiber orientation drive cancer cell polarity and migration along wavy ECM substrates. Proc. Natl. Acad. Sci. USA *118*, e2021135118. https://doi.org/10.1073/pnas.2021135118.
24. Harms, M.J., Li, Q., Lee, S., Zhang, C., Kull, B., Hallen, S., Thorell, A., Alexandersson, I., Hagberg, C.E., Peng, X.-R., et al. (2019). Mature Human White Adipocytes Cultured under Membranes Maintain Identity, Function, and Can Transdifferentiate into Brown-like Adipocytes. Cell Rep. *27*, 213–225.e5. https://doi.org/10.1016/j.celrep.2019.03.026.
25. Sugihara, H., Yonemitsu, N., Miyabara, S., and Yun, K. (1986). Primary cultures of unilocular fat cells: Characteristics of growth in vitro and changes in differentiation properties. Differentiation *31*, 42–49. https://doi.org/10.1111/j.1432-0436.1986.tb00381.x.
26. Wei, S., Bergen, W.G., Hausman, G.J., Zan, L., and Dodson, M.V. (2013). Cell culture purity issues and DFAT cells. Biochem. Biophys. Res. Commun. *433*, 273–275. https://doi.org/10.1016/j.bbrc.2013.03.006.
27. Shen, J.F., Sugawara, A., Yamashita, J., Ogura, H., and Sato, S. (2011). Dedifferentiated fat cells: An alternative source of adult multipotent cells from the adipose tissues. Int. J. Oral Sci. *3*, 117–124. https://doi.org/10.4248/IJOS11044.
28. Gesta, S., Lolmède, K., Daviaud, D., Berlan, M., Bouloumié, A., Lafontan, M., Valet, P., and Saulnier-Blache, J.S. (2003). Culture of human adipose tissue explants leads to profound alteration of adipocyte gene expression. Horm. Metab. Res. *35*, 158–163. https://doi.org/10.1055/s-2003-39070.
29. Caliari, S.R., and Burdick, J.A. (2016). A practical guide to hydrogels for cell culture. Nat. Methods *13*, 405–414. https://doi.org/10.1038/nmeth.3839.
30. Griffin, D.R., Weaver, W.M., Scumpia, P.O., Di Carlo, D., and Segura, T. (2015). Accelerated wound healing by injectable microporous gel scaffolds assembled from annealed building blocks. Nat. Mater. *14*, 737–744. https://doi.org/10.1038/nmat4294.
31. Qazi, T.H., Muir, V.G., and Burdick, J.A. (2022). Methods to Characterize Granular Hydrogel Rheological Properties, Porosity, and Cell Invasion. ACS Biomater. Sci. Eng. *8*, 1427–1442. https://doi.org/10.1021/acsbiomaterials.1c01440.
32. Hsu, C.-C., George, J.H., Waller, S., Besnard, C., Nagel, D.A., Hill, E.J., Coleman, M.D., Korsunsky, A.M., Cui, Z., and Ye, H. (2022). Increased connectivity of hiPSC-derived neural networks in multiphase granular hydrogel scaffolds. Bioact. Mater. *9*, 358–372. https://doi.org/10.1016/j.bioactmat.2021.07.008.
33. Zauchner, D., Müller, M.Z., Horrer, M., Bissig, L., Zhao, F., Fisch, P., Lee, S.S., Zenobi-Wong, M., Müller, R., and Qin, X.-H. (2024). Synthetic biodegradable microporous hydrogels for in vitro 3D culture of functional human bone cell networks. Nat. Commun. *15*, 5027. https://doi.org/10.1038/s41467-024-49280-3.
34. Asadikorayem, M., Brunel, L.G., Weber, P., Heilshorn, S.C., and Zenobi-Wong, M. (2024). Porosity dominates over microgel stiffness for promoting chondrogenesis in zwitterionic granular hydrogels. Biomater. Sci. *12*, 5504–5520. https://doi.org/10.1039/D4BM00233D.
35. Claxton, N.L., Luse, M.A., Isakson, B.E., and Highley, C.B. (2024). Engineering Granular Hydrogels without Interparticle Cross-Linking to Support Multicellular Organization. ACS Biomater. Sci. Eng. *10*, 7594–7605. https://doi.org/10.1021/acsbiomaterials.4c01563.
36. Shaik, R., Brown, J., Xu, J., Lamichhane, R., Wang, Y., Hong, Y., and Zhang, G. (2024). Cardiac Matrix-Derived Granular Hydrogel Enhances Cell Function in 3D Culture. ACS Appl. Mater. Interfaces *16*, 58346–58356. https://doi.org/10.1021/acsami.4c12871.
37. Riley, L., Schirmer, L., and Segura, T. (2019). Granular hydrogels: emergent properties of jammed hydrogel microparticles and their applications in tissue repair and regeneration. Curr. Opin. Biotechnol. *60*, 1–8. https://doi.org/10.1016/j.copbio.2018.11.001.
38. Romanazzo, S., Tian, P., Jalandhra, G.K., Doshi, R.B., Gooding, J.J., and Kilian, K.A. (2025). A biofabricated 3D cancer-stroma tumor microenvironment model. Biofabrication *17*, 045019. https://doi.org/10.1088/1758-5090/ae0a82.
39. Gonzalez-Molina, J., Nabili, P., Marciano, D., Abdelnabi, S., Gultekin, O., Rasul, M.F., Zhang, Y., Nadal, C., Chrysanthou, A., Alkasalias, T., et al. (2025). Biomimetic organo-hydrogels reveal the adipose tissue local mechanical anisotropy regulates ovarian cancer invasion. Nat. Commun. *16*, 8541. https://doi.org/10.1038/s41467-025-62296-7.
40. Zhang, I.W., Choi, L.S., Friend, N.E., McCoy, A.J., Midekssa, F.S., Hu, M.M., Alsberg, E., Lesher-Pérez, S.C., Stegemann, J.P., Baker, B.M., et al. (2025). Clickable PEG-norbornene microgels support suspension bioprinting and microvascular assembly. Acta Biomater. *201*, 283–296. https://doi.org/10.1016/j.actbio.2025.06.006.
41. Labriola, N.R., Mathiowitz, E., and Darling, E.M. (2016). Fabricating polyacrylamide microbeads by inverse emulsification to mimic the size and elasticity of living cells. Biomater. Sci. *5*, 41–45. https://doi.org/10.1039/C6BM00692B.
42. Girardo, S., Träber, N., Wagner, K., Cojoc, G., Herold, C., Goswami, R., Schlüßler, R., Abuhattum, S., Taubenberger, A., Reichel, F., et al. (2018). Standardized microgel beads as elastic cell mechanical probes. J. Mater. Chem. B *6*, 6245–6261. https://doi.org/10.1039/C8TB01421C.
43. Beeghly, G.F., Deng, J., and Fischbach, C. (2024). Protocol to fabricate elastomer microwells for three-dimensional culture of primary adipocytes. Star Protoc. *5*, 103264. https://doi.org/10.1016/j.xpro.2024.103264.
44. Shoham, N., Girshovitz, P., Katzengold, R., Shaked, N.T., Benayahu, D., and Gefen, A. (2014). Adipocyte Stiffness Increases with Accumulation of Lipid Droplets. Biophys. J. *106*, 1421–1431. https://doi.org/10.1016/j.bpj.2014.01.045.
45. Darling, E.M., Topel, M., Zauscher, S., Vail, T.P., and Guilak, F. (2008). Viscoelastic properties of human mesenchymally-derived stem cells and primary osteoblasts, chondrocytes, and adipocytes. J. Biomech. *41*, 454–464. https://doi.org/10.1016/j.jbiomech.2007.06.019.
46. Milos, F., and del Campo, A. (2024). Polyacrylamide Hydrogels as Versatile Biomimetic Platforms to Study Cell-Materials Interactions. Adv. Materials Inter. *11*, 2400404. https://doi.org/10.1002/admi.202400404.
47. Shi, X., and Janmey, P.A. (2023). Large Polyacrylamide Hydrogels for Large-Batch Cell Culture and Mechanobiological Studies. Macromol. Biosci. *23*, e2300042. https://doi.org/10.1002/mabi.202300042.
48. Provenzano, P.P., Eliceiri, K.W., Campbell, J.M., Inman, D.R., White, J.G., and Keely, P.J. (2006). Collagen reorganization at the tumor-stromal interface facilitates local invasion. BMC Med. *4*, 38. https://doi.org/10.1186/1741-7015-4-38.
49. Rosin, N.L., Winstone, T.M.L., Kelley, M., Biernaskie, J., Dufour, A., and Orton, D.J. (2024). Targeted proteomic approach for quantification of collagen type I and type III in formalin-fixed paraffin-embedded tissue. Sci. Rep. *14*, 17769. https://doi.org/10.1038/s41598-024-68377-9.
50. Kakkad, S.M., Solaiyappan, M., Argani, P., Sukumar, S., Jacobs, L.K., Leibfritz, D., Bhujwalla, Z.M., and Glunde, K. (2012). Collagen I fiber density increases in lymph node positive breast cancers: pilot study. J. Biomed. Opt. *17*, 116017. https://doi.org/10.1117/1.JBO.17.11.116017.

51. Lu, P., Weaver, V.M., and Werb, Z. (2012). The extracellular matrix: A dynamic niche in cancer progression. J. Cell Biol. *196*, 395–406. https://doi.org/10.1083/jcb.201102147.

52. Sapudom, J., and Pompe, T. (2018). Biomimetic tumor microenvironments based on collagen matrices. Biomater. Sci. *6*, 2009–2024. https://doi.org/10.1039/C8BM00303C.

53. Seo, B.R., Chen, X., Ling, L., Song, Y.H., Shimpi, A.A., Choi, S., Gonzalez, J., Sapudom, J., Wang, K., Andresen Eguiluz, R.C., et al. (2020). Collagen microarchitecture mechanically controls myofibroblast differentiation. Proc. Natl. Acad. Sci. USA *117*, 11387–11398. https://doi.org/10.1073/pnas.1919394117.

54. Jaberi, A., Kedzierski, A., Kheirabadi, S., Tagay, Y., Ataie, Z., Zavari, S., Naghashnejad, M., Waldron, O., Adhikari, D., Lester, G., et al. (2024). Engineering Microgel Packing to Tailor the Physical and Biological Properties of Gelatin Methacryloyl Granular Hydrogel Scaffolds. Adv. Healthc. Mater. *13*, e2402489. https://doi.org/10.1002/adhm.202402489.

55. Alkhouli, N., Mansfield, J., Green, E., Bell, J., Knight, B., Liversedge, N., Tham, J.C., Welbourn, R., Shore, A.C., Kos, K., et al. (2013). The mechanical properties of human adipose tissues and their relationships to the structure and composition of the extracellular matrix. Am. J. Physiol., Endocrinol. Metab. *305*, E1427–E1435. https://doi.org/10.1152/ajpendo.00111.2013.

56. Legant, W.R., Miller, J.S., Blakely, B.L., Cohen, D.M., Genin, G.M., and Chen, C.S. (2010). Measurement of mechanical tractions exerted by cells in three-dimensional matrices. Nat. Methods *7*, 969–971. https://doi.org/10.1038/nmeth.1531.

57. Chaudhuri, O., Gu, L., Klumpers, D., Darnell, M., Bencherif, S.A., Weaver, J.C., Huebsch, N., Lee, H.P., Lippens, E., Duda, G.N., et al. (2016). Hydrogels with tunable stress relaxation regulate stem cell fate and activity. Nat. Mater. *15*, 326–334. https://doi.org/10.1038/nmat4489.

58. Beeghly, G.F., Amofa, K.Y., Fischbach, C., and Kumar, S. (2022). Regulation of Tumor Invasion by the Physical Microenvironment: Lessons from Breast and Brain Cancer. Annu. Rev. Biomed. Eng. *24*, 29–59. https://doi.org/10.1146/annurev-bioeng-110220-115419.

59. Huda, S., Weigelin, B., Wolf, K., Tretiakov, K.V., Polev, K., Wilk, G., Iwasa, M., Emami, F.S., Narojczyk, J.W., Banaszak, M., et al. (2018). Lévy-like movement patterns of metastatic cancer cells revealed in microfabricated systems and implicated in vivo. Nat. Commun. *9*, 4539. https://doi.org/10.1038/s41467-018-06563-w.

60. Riching, K.M., Cox, B.L., Salick, M.R., Pehlke, C., Riching, A.S., Ponik, S.M., Bass, B.R., Crone, W.C., Jiang, Y., Weaver, A.M., et al. (2014). 3D Collagen Alignment Limits Protrusions to Enhance Breast Cancer Cell Persistence. Biophys. J. *107*, 2546–2558. https://doi.org/10.1016/j.bpj.2014.10.035.

61. Conklin, M.W., Eickhoff, J.C., Riching, K.M., Pehlke, C.A., Eliceiri, K.W., Provenzano, P.P., Friedl, A., and Keely, P.J. (2011). Aligned Collagen Is a Prognostic Signature for Survival in Human Breast Carcinoma. Am. J. Pathol. *178*, 1221–1232. https://doi.org/10.1016/j.ajpath.2010.11.076.

62. Kayser, J., Grabmayr, H., Harasim, M., Herrmann, H., and Bausch, A.R. (2012). Assembly kinetics determine the structure of keratin networks. Soft Matter *8*, 8873–8879. https://doi.org/10.1039/C2SM26032H.

63. Püspöki, Z., Storath, M., Sage, D., and Unser, M. (2016). Transforms and Operators for Directional Bioimage Analysis: A Survey. Adv. Anat. Embryol. Cell Biol. *219*, 69–93. https://doi.org/10.1007/978-3-319-28549-8_3.

64. Rycroft, C.H. (2009). VORO++: A three-dimensional Voronoi cell library in C++. Chaos *19*, 041111. https://doi.org/10.1063/1.3215722.

65. Choi, J., Rakhilin, N., Gadamsetty, P., Joe, D.J., Tabrizian, T., Lipkin, S.M., Huffman, D.M., Shen, X., and Nishimura, N. (2018). Intestinal crypts recover rapidly from focal damage with coordinated motion of stem cells that is impaired by aging. Sci. Rep. *8*, 10989. https://doi.org/10.1038/s41598-018-29230-y.

66. An, L., Kim, D., Donahue, L.R., Mejooli, M.A., Eom, C.-Y., Nishimura, N., and White, A.C. (2024). Sexual dimorphism in melanocyte stem cell behavior reveals combinational therapeutic strategies for cutaneous repigmentation. Nat. Commun. *15*, 796. https://doi.org/10.1038/s41467-024-45034-3.

67. Desjardins-Lecavalier, N., Annis, M.G., Nowakowski, A., Kiepas, A., Binan, L., Roy, J., Modica, G., Hébert, S., Kleinman, C.L., Siegel, P.M., et al. (2023). Migration speed of captured breast cancer subpopulations correlates with metastatic fitness. J. Cell Sci. *136*, jcs260835. https://doi.org/10.1242/jcs.260835.

68. Mistriotis, P., Wisniewski, E.O., Bera, K., Keys, J., Li, Y., Tuntithavornwat, S., Law, R.A., Perez-Gonzalez, N.A., Erdogmus, E., Zhang, Y., et al. (2019). Confinement hinders motility by inducing RhoA-mediated nuclear influx, volume expansion, and blebbing. J. Cell Biol. *218*, 4093–4111. https://doi.org/10.1083/jcb.201902057.

69. McGregor, A.L., Hsia, C.-R., and Lammerding, J. (2016). Squish and squeeze—the nucleus as a physical barrier during migration in confined environments. Curr. Opin. Cell Biol. *40*, 32–40. https://doi.org/10.1016/j.ceb.2016.01.011.

70. Paul, C.D., Mistriotis, P., and Konstantopoulos, K. (2017). Cancer cell motility: lessons from migration in confined spaces. Nat. Rev. Cancer *17*, 131–140. https://doi.org/10.1038/nrc.2016.123.

71. Caswell, P.T., and Zech, T. (2018). Actin-Based Cell Protrusion in a 3D Matrix. Trends Cell Biol. *28*, 823–834. https://doi.org/10.1016/j.tcb.2018.06.003.

72. Krause, M., Yang, F.W., te Lindert, M., Isermann, P., Schepens, J., Maas, R.J.A., Venkataraman, C., Lammerding, J., Madzvamuse, A., Hendriks, W., et al. (2019). Cell migration through three-dimensional confining pores: speed accelerations by deformation and recoil of the nucleus. Philos. Trans. R. Soc. Lond. B Biol. Sci. *374*, 20180225. https://doi.org/10.1098/rstb.2018.0225.

73. Xia, Y., Pfeifer, C.R., and Discher, D.E. (2019). Nuclear mechanics during and after constricted migration. Acta Mech. Sin. *35*, 299–308. https://doi.org/10.1007/s10409-018-00836-9.

74. Swaminathan, V., Mythreye, K., O'Brien, E.T., Berchuck, A., Blobe, G.C., and Superfine, R. (2011). Mechanical stiffness grades metastatic potential in patient tumor cells and in cancer cell lines. Cancer Res. *71*, 5075–5080. https://doi.org/10.1158/0008-5472.CAN-11-0247.

75. Alibert, C., Goud, B., and Manneville, J.-B. (2017). Are cancer cells really softer than normal cells? Biol. Cell *109*, 167–189. https://doi.org/10.1111/boc.201600078.

76. Liu, G.Y., Agarwal, R., Ko, K.R., Ruthven, M., Sarhan, H.T., and Frampton, J.P. (2017). Templated Assembly of Collagen Fibers Directs Cell Growth in 2D and 3D. Sci. Rep. *7*, 9628. https://doi.org/10.1038/s41598-017-10182-8.

77. Dudaryeva, O.Y., Bucciarelli, A., Bovone, G., Huwyler, F., Jaydev, S., Broguiere, N., Al-Bayati, M., Lütolf, M., and Tibbitt, M.W. (2021). 3D Confinement Regulates Cell Life and Death. Adv. Funct. Materials *31*, 2104098. https://doi.org/10.1002/adfm.202104098.

78. Shen, Q., Hill, T., Cai, X., Bui, L., Barakat, R., Hills, E., Almugaiteeb, T., Babu, A., Mckernan, P.H., Zalles, M., et al. (2021). Physical Confinement during Cancer Cell Migration Triggers Therapeutic Resistance and Cancer Stem Cell-like Behavior. Cancer Lett. *506*, 142–151. https://doi.org/10.1016/j.canlet.2021.01.020.

79. Qu, F., Li, Q., Wang, X., Cao, X., Zgonis, M.H., Esterhai, J.L., Shenoy, V.B., Han, L., and Mauck, R.L. (2018). Maturation State and Matrix Microstructure Regulate Interstitial Cell Migration in Dense Connective Tissues. Sci. Rep. *8*, 3295. https://doi.org/10.1038/s41598-018-21212-4.

80. Zaman, M.H., Trapani, L.M., Sieminski, A.L., MacKellar, D., Gong, H., Kamm, R.D., Wells, A., Lauffenburger, D.A., and Matsudaira, P. (2006). Migration of tumor cells in 3D matrices is governed by matrix stiffness along with cell-matrix adhesion and proteolysis. Proc. Natl. Acad. Sci. USA *103*, 10889–10894. https://doi.org/10.1073/pnas.0604460103.

81. Berger, A.J., Renner, C.M., Hale, I., Yang, X., Ponik, S.M., Weisman, P.S., Masters, K.S., and Kreeger, P.K. (2020). Scaffold stiffness influences breast cancer cell invasion via EGFR-linked Mena upregulation and matrix remodeling. Matrix Biol. *85*, 80–93. https://doi.org/10.1016/j.matbio.2019.07.006.

82. Friedl, P., and Alexander, S. (2011). Cancer Invasion and the Microenvironment: Plasticity and Reciprocity. Cell *147*, 992–1009. https://doi.org/10.1016/j.cell.2011.11.016.

83. Ranamukhaarachchi, S.K., Modi, R.N., Han, A., Velez, D.O., Kumar, A., Engler, A.J., and Fraley, S.I. (2019). Macromolecular crowding tunes 3D collagen architecture and cell morphogenesis. Biomater. Sci. *7*, 618–633. https://doi.org/10.1039/C8BM01188E.

84. Saeidi, N., Karmelek, K.P., Paten, J.A., Zareian, R., DiMasi, E., and Ruberti, J.W. (2012). Molecular crowding of collagen: A pathway to produce highly-organized collagenous structures. Biomaterials *33*, 7366–7374. https://doi.org/10.1016/j.biomaterials.2012.06.041.

85. Joorabi, F.T., Derr, N.J., Li, Z., Nerger, B.A., Rycroft, C.H., Mooney, D.J., and Vining, K.H. (2025). Mechanical cues of an interpenetrating polysaccharide matrix regulate self-assembly of collagen fibers. Preprint at bioRxiv. https://doi.org/10.64898/2025.11.28.691198.

86. Fraley, S.I., Wu, P.H., He, L., Feng, Y., Krisnamurthy, R., Longmore, G.D., and Wirtz, D. (2015). Three-dimensional matrix fiber alignment modulates cell migration and MT1-MMP utility by spatially and temporally directing protrusions. Sci. Rep. *5*, 14580. https://doi.org/10.1038/srep14580.

87. Niraula, G., Foroozandehfar, A., Namanda, F.R., and Schneider, I.C. (2025). Aligned Collagen Fibers Drive Distinct Traction Force Signatures to Regulate Contact Guidance. ACS Nano *19*, 30165–30185. https://doi.org/10.1021/acsnano.5c06736.

88. Dahl, K.N., Ribeiro, A.J.S., and Lammerding, J. (2008). Nuclear Shape, Mechanics, and Mechanotransduction. Circ. Res. *102*, 1307–1318. https://doi.org/10.1161/CIRCRESAHA.108.173989.

89. Isermann, P., and Lammerding, J. (2017). Consequences of a tight squeeze: Nuclear envelope rupture and repair. Nucleus *8*, 268–274. https://doi.org/10.1080/19491034.2017.1292191.

90. Wang, Z., Xu, F., Wu, D., Huang, W., Chu, Z., and Lin, Y. (2025). Nuclear Deformation and Stiffness-Dependent Traction Force Generation Dictate the Migration of Cells under Confinement. ACS Appl. Mater. Interfaces *17*, 23731–23739. https://doi.org/10.1021/acsami.5c03048.

91. Hockenberry, M.A., Ulmer, A.J., Rapp, J.L., Truscott, H.H., Leibfarth, F.A., Bear, J.E., and Legant, W.R. (2025). Measurement of cellular traction forces during confined migration. Proc. Natl. Acad. Sci. USA *122*, e2509535122. https://doi.org/10.1073/pnas.2509535122.

92. Gensbittel, V., Follain, G., Bochler, L., Uhlmann, K., Lefèbvre, O., Larnicol, A., Harlepp, S., Goswami, R., Girardo, S., Hyenne, V., et al. (2026). Cell viscosity influences hematogenous dissemination and metastatic extravasation of tumor cells. Nature materials *25*, 1–12. https://doi.org/10.1101/2024.03.28.587171.

93. Wang, W.Y., Pearson, A.T., Kutys, M.L., Choi, C.K., Wozniak, M.A., Baker, B.M., and Chen, C.S. (2018). Extracellular matrix alignment dictates the organization of focal adhesions and directs uniaxial cell migration. APL Bioeng. *2*, 046107. https://doi.org/10.1063/1.5052239.

94. Wong, K.S., Zhong, X., Low, C.S.L., and Kanchanawong, P. (2022). Self-supervised classification of subcellular morphometric phenotypes reveals extracellular matrix-specific morphological responses. Sci. Rep. *12*, 15329. https://doi.org/10.1038/s41598-022-19472-2.

95. Beunk, L., Bakker, G.-J., van Ens, D., Bugter, J., Gal, F., Svoren, M., Friedl, P., and Wolf, K. (2022). Actomyosin contractility requirements and reciprocal cell–tissue mechanics for cancer cell invasion through collagen-based channels. Eur. Phys. J. E Soft Matter *45*, 48. https://doi.org/10.1140/epje/s10189-022-00182-6.

96. Duxbury, M.S., Ashley, S.W., and Whang, E.E. (2004). Inhibition of pancreatic adenocarcinoma cellular invasiveness by blebbistatin: a novel myosin II inhibitor. Biochem. Biophys. Res. Commun. *313*, 992–997. https://doi.org/10.1016/j.bbrc.2003.12.031.

97. Nader, G.P. de F., Agüera-Gonzalez, S., Routet, F., Gratia, M., Maurin, M., Cancila, V., Cadart, C., Palamidessi, A., Ramos, R.N., San Roman, M., et al. (2021). Compromised nuclear envelope integrity drives TREX1-dependent DNA damage and tumor cell invasion. Cell *184*, 5230–5246.e22. https://doi.org/10.1016/j.cell.2021.08.035.

98. Kedrin, D., Gligorijevic, B., Wyckoff, J., Verkhusha, V.V., Condeelis, J., Segall, J.E., and van Rheenen, J. (2008). Intravital imaging of metastatic behavior through a mammary imaging window. Nat. Methods *5*, 1019–1021. https://doi.org/10.1038/nmeth.1269.

99. Ilina, O., Campanello, L., Gritsenko, P.G., Vullings, M., Wang, C., Bult, P., Losert, W., and Friedl, P. (2018). Intravital microscopy of collective invasion plasticity in breast cancer. Dis. Model. Mech. *11*, dmm034330. https://doi.org/10.1242/dmm.034330.

100. He, X., and Jiang, Y. (2017). Substrate curvature regulates cell migration. Phys. Biol. *14*, 035006. https://doi.org/10.1088/1478-3975/aa6f8e.

101. Nguyen, R.Y., Cabral, A.T., Rossello-Martinez, A., Zulli, A., Gong, X., Zhang, Q., Yan, J., and Mak, M. (2023). Tunable Mesoscopic Collagen Island Architectures Modulate Stem Cell Behavior. Adv. Mater. *35*, e2207882. https://doi.org/10.1002/adma.202207882.

102. Blade, S.P., Falkowski, D.J., Bachand, S.N., Pagano, S.J., and Chin, L. (2024). Mechanobiology of Adipocytes. Biology *13*, 434. https://doi.org/10.3390/biology13060434.

103. Pérez-Calixto, D., Amat-Shapiro, S., Zamarrón-Hernández, D., Vázquez-Victorio, G., Puech, P.-H., and Hautefeuille, M. (2021). Determination by Relaxation Tests of the Mechanical Properties of Soft Polyacrylamide Gels Made for Mechanobiology Studies. Polymers *13*, 629. https://doi.org/10.3390/polym13040629.

104. Charbonier, F., Indana, D., and Chaudhuri, O. (2021). Tuning viscoelasticity in alginate hydrogels for 3D cell culture studies. Curr. Protoc. *1*, e124. https://doi.org/10.1002/cpz1.124.

105. Rouwkema, J., Koopman, B.F.J.M., Blitterswijk, C.A.V., Dhert, W.J.A., and Malda, J. (2010). Supply of Nutrients to Cells in Engineered Tissues. Biotechnol. Genet. Eng. Rev. *26*, 163–178. https://doi.org/10.5661/bger-26-163.

106. Wolf, K., te Lindert, M., Krause, M., Alexander, S., Te Riet, J., Willis, A.L., Hoffman, R.M., Figdor, C.G., Weiss, S.J., and Friedl, P. (2013). Physical limits of cell migration: Control by ECM space and nuclear deformation and tuning by proteolysis and traction force. J. Cell Biol. *201*, 1069–1084. https://doi.org/10.1083/jcb.201210152.

107. Friedl, P., and Wolf, K. (2009). Proteolytic interstitial cell migration: a five-step process. Cancer Metastasis Rev. *28*, 129–135. https://doi.org/10.1007/s10555-008-9174-3.

108. Beunk, L., Wen, N., van Helvert, S., Bekker, B., Ran, L., Kang, R., Paulat, T., Syga, S., Deutsch, A., Friedl, P., et al. (2023). Cell jamming in a collagen-based interface assay is tuned by collagen density and proteolysis. J. Cell Sci. *136*, jcs260207. https://doi.org/10.1242/jcs.260207.

109. Duong, M.N., Geneste, A., Fallone, F., Li, X., Dumontet, C., and Muller, C. (2017). The fat and the bad: Mature adipocytes, key actors in tumor progression and resistance. Oncotarget *8*, 57622–57641. https://doi.org/10.18632/oncotarget.18038.

110. Luo, Y., Chen, G.-L., Hannemann, N., Ipseiz, N., Krönke, G., Bäuerle, T., Munos, L., Wirtz, S., Schett, G., and Bozec, A. (2015). Microbiota from Obese Mice Regulate Hematopoietic Stem Cell Differentiation by Altering the Bone Niche. Cell Metab. *22*, 886–894. https://doi.org/10.1016/j.cmet.2015.08.020.

111. Glaubitz, M., Medvedev, N., Pussak, D., Hartmann, L., Schmidt, S., Helm, C.A., and Delcea, M. (2014). A novel contact model for AFM indentation experiments on soft spherical cell-like particles. Soft Matter *10*, 6732–6741. https://doi.org/10.1039/C4SM00788C.

112. Rengarajan, V., Clyde, A., Pontsler, J., Valiente, J., Peel, A., and Huang, Y. (2023). Assessing Leachable Cytotoxicity of 3D-Printed Polymers and

Facile Detoxification Methods. 3D Print. Addit. Manuf. *10*, 1110–1121. https://doi.org/10.1089/3dp.2021.0216.

113. Carter, S.-S.D., Atif, A.-R., Kadekar, S., Lanekoff, I., Engqvist, H., Varghese, O.P., Tenje, M., and Mestres, G. (2020). PDMS leaching and its implications for on-chip studies focusing on bone regeneration applications. Organs-on-a-Chip *2*, 100004. https://doi.org/10.1016/j.ooc.2020.100004.

114. de Almeida Monteiro Melo Ferraz, M., Nagashima, J.B., Venzac, B., Le Gac, S., and Songsasen, N. (2020). 3D printed mold leachates in PDMS microfluidic devices. Sci. Rep. *10*, 994. https://doi.org/10.1038/s41598-020-57816-y.

115. Antoine, E.E., Vlachos, P.P., and Rylander, M.N. (2014). Review of Collagen I Hydrogels for Bioengineered Tissue Microenvironments: Characterization of Mechanics, Structure, and Transport. Tissue Eng. Part B Rev. *20*, 683–696. https://doi.org/10.1089/ten.teb.2014.0086.

116. Baltazar, T., Kajave, N.S., Rodriguez, M., Chakraborty, S., Jiang, B., Skardal, A., Kishore, V., Pober, J.S., and Albanna, M.Z. (2022). Native human collagen type I provides a viable physiologically relevant alternative to xenogeneic sources for tissue engineering applications: A comparative in vitro and in vivo study. J. Biomed. Mater. Res., B *110*, 2323–2337. https://doi.org/10.1002/jbm.b.35080.

117. Nam, S., Hu, K.H., Butte, M.J., and Chaudhuri, O. (2016). Strain-enhanced stress relaxation impacts nonlinear elasticity in collagen gels. Proc. Natl. Acad. Sci. USA *113*, 5492–5497. https://doi.org/10.1073/pnas.1523906113.

118. Shen, Z.L., Kahn, H., Ballarini, R., and Eppell, S.J. (2011). Viscoelastic Properties of Isolated Collagen Fibrils. Biophys. J. *100*, 3008–3015. https://doi.org/10.1016/j.bpj.2011.04.052.

119. Schindelin, J., Arganda-Carreras, I., Frise, E., Kaynig, V., Longair, M., Pietzsch, T., Preibisch, S., Rueden, C., Saalfeld, S., Schmid, B., et al. (2012). Fiji: an open-source platform for biological-image analysis. Nat. Methods *9*, 676–682. https://doi.org/10.1038/nmeth.2019.

120. Kim, D.-H., and Wirtz, D. (2013). Focal adhesion size uniquely predicts cell migration. FASEB J. *27*, 1351–1361. https://doi.org/10.1096/fj.12-220160.

121. Marcotti, S., de Freitas, D.B., Troughton, L.D., Kenny, F.N., Shaw, T.J., Stramer, B.M., and Oakes, P.W. (2021). A Workflow for Rapid Unbiased Quantification of Fibrillar Feature Alignment in Biological Images. Front. Comput. Sci. *3*, 745831. https://doi.org/10.3389/fcomp.2021.745831.

122. Liu, Y., Keikhosravi, A., Pehlke, C.A., Bredfeldt, J.S., Dutson, M., Liu, H., Mehta, G.S., Claus, R., Patel, A.J., Conklin, M.W., et al. (2020). Fibrillar Collagen Quantification With Curvelet Transform Based Computational Methods. Front. Bioeng. Biotechnol. *8*, 198. https://doi.org/10.3389/fbioe.2020.00198.

123. Schmidt, U., Weigert, M., Broaddus, C., and Myers, G. (2018). Cell Detection with Star-Convex Polygons. In Medical Image Computing and Computer Assisted Intervention – MICCAI 2018, A.F. Frangi, J.A. Schnabel, C. Davatzikos, C. Alberola-López, and G. Fichtinger, eds. (Springer International Publishing), pp. 265–273. https://doi.org/10.1007/978-3-030-00934-2_30.

124. Tinevez, J.-Y., Perry, N., Schindelin, J., Hoopes, G.M., Reynolds, G.D., Laplantine, E., Bednarek, S.Y., Shorte, S.L., and Eliceiri, K.W. (2017). TrackMate: An open and extensible platform for single-particle tracking. Methods *115*, 80–90. https://doi.org/10.1016/j.ymeth.2016.09.016.

125. Crocker, J.C., and Grier, D.G. (1996). Methods of Digital Video Microscopy for Colloidal Studies. J. Colloid Interface Sci. *179*, 298–310. https://doi.org/10.1006/jcis.1996.0217.

126. Tat, M.E., Van Gerpen, J.H., Soylu, S., Canakci, M., Monyem, A., and Wormley, S. (2000). The speed of sound and isentropic bulk modulus of biodiesel at 21°C from atmospheric pressure to 35 MPa. J. Am. Oil Chem. Soc. *77*, 285–289. https://doi.org/10.1007/s11746-000-0047-z.